Monthly Notices of the ROYAL ASTRONOMICAL SOCIETY

MNRAS **520,** 5783–5802 (2023) https://doi.org/10.1093/mnras/stad439
Advance Access publication 2023 February 9

SUPER VII. morphology and kinematics of H α emission in AGN host galaxies at cosmic noon using SINFONI

D. Kakkad [1,2,3]★ V. Mainieri,[4] G. Vietri,[5,6] I. Lamperti [7] S. Carniani [8] G. Cresci,[9] C. Harrison [10] A. Marconi,[9,11] M. Bischetti,[12,13] C. Cicone,[14] C. Circosta,[15,16] B. Husemann [17] A. Man [18,19] F. Mannucci [9] H. Netzer [20] P. Padovani [4,21] M. Perna,[7,9] A. Puglisi [22] J. Scholtz [23,24] G. Tozzi [11,9] C. Vignali[25,26] and L. Zappacosta[5]

Affiliations are listed at the end of the paper

Accepted 2023 January 31. Received 2022 December 24; in original form 2022 September 30

ABSTRACT

We present spatially resolved H α properties of 21 type 1 AGN host galaxies at z $\sim$ 2 derived from the SUPER survey. These targets were observed with the adaptive optics capabilities of the SINFONI spectrograph, a near-infrared integral field spectrograph, that provided a median spatial resolution of 0.3 arcsec ($\sim$2 kpc). We model the H α emission line profile in each pixel to investigate whether it traces gas in the narrow line region or if it is associated with star formation. To do this, we first investigate the presence of resolved H α emission after subtracting the AGN PSF. We find extended H α emission in 16 out of the 21 type 1 AGN host galaxies (76 per cent). Based on the BPT diagnostics, optical line flux ratios and line widths (FWHM), we show that the H α emission in five galaxies is ionized by the AGN (30 per cent), in four galaxies by star formation (25 per cent) and for the rest (45 per cent), the ionization source is unconstrained. Two galaxies show extended H α FWHM $>$600 km s^{-1}, which is interpreted as a part of an AGN-driven outflow. Morphological and kinematic maps of H α emission in targets with sufficient signal-to-noise ratio suggest the presence of rotationally supported discs in six galaxies and possible presence of companions in four galaxies. In two galaxies, we find an anticorrelation between the locations of extended H α emission and [O III]-based ionized outflows, indicating possible negative feedback at play. However, in the majority of galaxies, we do not find evidence of outflows impacting H α-based star formation.

Key words: galaxies: active – galaxies: evolution – galaxies: high-redshift – galaxies: kinematics and dynamics – quasars: supermassive black holes – galaxies: star formation.

1 INTRODUCTION

The conventional Λ cold dark matter (ΛCDM) paradigm supports a hierarchical growth of objects, i.e. smaller objects are formed first, then they merge successively into larger bodies. Within this picture, stars and galaxies are formed when baryons fall into dark matter potential wells, resulting in shocks followed by radiative cooling of gas (e.g. White & Rees 1978; Hopkins & Beacom 2006). Although this paradigm had initial success to describe a cosmological model for galaxy evolution, feedback processes needed to be invoked to regulate the formation of stars in the interstellar medium (ISM). One of the prominent sources of feedback in massive galaxies comes from the centrally located supermassive black holes (e.g. Kormendy & Richstone 1995; Richstone et al. 1998; Silk & Rees 1998).

Models predict that the feedback from these black holes is a result of radio jets and/or radiation pressure driven winds from the accretion of gas and dust from the ISM (e.g. Soltan 1982; Yu & Tremaine 2002; Fabian 2012). During the accretion process, the luminosity of these black holes, also called active galactic nuclei (AGN) at this stage, can outshine the overall luminosity of the host galaxy itself. The net effect of these winds could be to relocate or eject cold molecular gas from the galaxy, dissociate or heat this gas and/or possibly prevent the inflow of gas from the halo into the ISM. Feedback processes from both star formation and AGN are largely used in state-of-the-art cosmological simulations (e.g. Springel 2005; Hirschmann et al. 2014; Vogelsberger et al. 2014; Schaye et al. 2015; Steinborn et al. 2015; Dubois et al. 2016; Pillepich et al. 2018). An indirect manifestation of the influence that the AGN has on the growth history of its host galaxy is represented by the observed AGN-galaxy correlations, such as the black hole mass versus the stellar velocity dispersion ($M_{\rm BH} - \sigma$) and the black hole mass and bulge mass relation ($M_{\rm BH} - M_{\rm bulge}$) (e.g. Gebhardt et al. 2000; Gültekin et al. 2009; Caglar et al. 2020).

Spectroscopic observations of AGN host galaxies over the past decades have revealed the ubiquitous presence of fast outflows with speeds $>$1000 km s^{-1} in multiple gas phases across a wide range of redshifts (e.g. Greene et al. 2011; Venturi et al. 2018; Rojas et al. 2020; Perna et al. 2021; Puglisi et al. 2021; Ramos Almeida et al. 2021; Tozzi et al. 2021; Gatkine et al. 2022). Several studies found that these outflows are either driven by the AGN or star formation, based on the presence of correlations between the outflow and AGN or host galaxy properties (e.g. Carniani et al. 2015; Fiore et al. 2017;

★ E-mail: darshankakkad@gmail.com

Fluetsch et al. 2019; Kakkad et al. 2022). However, there are also studies with different samples that report the absence of such scaling relations (e.g. Baron et al. 2020; Davies et al. 2020).

To investigate the feedback effects generated by these outflows, we can study direct or indirect tracers of the host galaxy's molecular gas supply and/or star formation. Several studies in the literature have investigated the overall content and distribution of cold molecular gas with some results suggesting a systematic difference in the molecular gas fractions between AGN and non-AGN galaxies (e.g. Kakkad et al. 2017; Brusa et al. 2018; Circosta et al. 2021; Ellison et al. 2021), while several others (mostly at low redshift) do not find the same result (e.g. Husemann et al. 2017; Rosario et al. 2018; Jarvis et al. 2020; Koss et al. 2021). The molecular gas observations described above have the limitation that the results are mostly based on individual tracers [such as CO(2-1)], which can give an incomplete view into the ISM because the molecular gas itself can exist in multiple phases or can be traced via different excitation levels of CO. Furthermore, most of these studies do not spatially resolve the molecular gas as the CO measurements are obtained from integrated apertures. Lastly, the apertures of extraction are not always uniform which leads to conflicting results in the literature.

Whether the outflows from the AGN have an impact on the host galaxy or not can also be revealed by investigating their impact on star formation (see review by Harrison et al. 2018 and references therein). Cosmological simulations predict a diverse set of scenarios where the star formation is regulated by the AGN, which may not result in an obvious observational signature of this feedback effect on the host galaxies of the AGN population (e.g. Ward et al. 2022). We briefly mention some examples here and we refer the reader to the references for further details. Using RAMSES-RT code, Costa et al. (2018) show that the outflows have the possibility to quench overall star formation (see also Dubois et al. 2013; Beckmann et al. 2017). Similar results are obtained in other suite of codes where the outflows have been shown to prevent the formation of new stars rather than shutting down ongoing star formation as a mechanism of quenching (e.g. Pillepich et al. 2018). On the other hand, Zubovas et al. (2013a) show that it is possible even for stars to be ejected from the host galaxies, when dense shells formed due to the shocks and compression from impact of AGN outflows form stars along a radial trajectory. Such pressure-regulated star formation has been reported in several theoretical studies and high resolution hydrodynamical simulations (e.g. Ishibashi & Fabian 2012; Silk 2013; Zubovas et al. 2013b; Dugan et al. 2014; Bieri et al. 2016). The burst of star formation is then followed by a period of quenching. Therefore, the AGN outflows could have the simultaneous capability of both suppressing and enhancing star formation (e.g. Zubovas & Bourne 2017). We also note that some of the results from the literature also report conditions where these outflows show limited impact of AGN feedback on the gas and star formation in the disc (e.g. Gabor & Bournaud 2014; Roos et al. 2015). In summary, simulations predict several possible scenarios on the impact of outflows on star formation and that there is no universal answer to how exactly AGN feedback regulates star formation for each galaxy.

The results from theory and simulations reported above can perhaps explain the diversity in the results, and often conflicting ones, from an observational perspective (see review on positive and negative feedback in AGN host galaxies; Cresci & Maiolino 2018). Gas ejection by AGN winds or star formation quenching in AGN host galaxies has been reported in several low-redshift and high-redshift galaxies (e.g. Cano-Díaz et al. 2012; Alatalo et al. 2015; Guillard et al. 2015; Carniani et al. 2016; Baron et al. 2018; George et al. 2019). Similar to the predictions made in Pillepich et al. (2018), using VLT/XSHOOTER and ALMA observations of a z $\sim$ 2.5 massive radio galaxy, Man et al. (2019) reported that most of the molecular gas is consumed by stars, followed by the removal of residual gas by the AGN. On the other hand, positive feedback has also been observed in the extragalactic sources, including dwarf galaxies (e.g. Gaibler et al. 2012; Rauch et al. 2013; Salomé, Salomé & Combes 2015; Maiolino et al. 2017; Gallagher et al. 2019; Nesvadba et al. 2020; Perna et al. 2020; Bessiere & Ramos Almeida 2022; Schutte & Reines 2022), with some targets that show a simultaneous presence of positive and negative feedback via spatially resolved integral field spectroscopic observations at rest-frame optical wavelengths (e.g. Cresci et al. 2015; Shin et al. 2019). Not all AGN host galaxies with outflows show the impact of star formation suppression or enhancement, especially when accounting for studies that make use of integrated spectra (i.e. a global outlook into the outflows versus star formation paradigm; Balmaverde et al. 2016) or when considering dust obscured star formation (e.g. Scholtz et al. 2020; Lamperti et al. 2021; Scholtz et al. 2021). Indeed, the presence of negative or positive feedback in AGN depends upon the conditions of the ISM, outflows, and/or jet power (e.g. Kalfountzou et al. 2017), which could also explain the diverse sets of results reported in the literature on the observational front.

Lastly, star formation itself can be calculated via multiple methods, each tracing different time-scales of star formation (e.g. Kennicutt 1998; Battisti et al. 2015; Boquien et al. 2015; Catalán-Torrecilla et al. 2015; Xie & Ho 2019; Calzetti 2020; Michiyama et al. 2020; Kim et al. 2022; Vietri et al. 2022). Furthermore, the results may further change depending on whether spatially resolved or integrated spectral measurements were made. For instance, star formation rate (SFR) calculated from the rest-frame ultraviolet wavelengths probe direct stellar light, while SFR calculated from the far-infrared wavelengths probes stellar light reprocessed by the dust (e.g. Shivaei et al. 2016). In the examples mentioned above, Hα is often used as a star formation tracer for many extragalactic studies. Although the Hα line might be a reliable tracer in normal star forming galaxies across a wide range of redshifts, in the AGN host galaxies, there is a possibility of contamination by the AGN ionization. Furthermore, we note that emission in FUV or optical wavelengths trace unobscured star formation and therefore dust obscuration effects need to be accounted for to get a complete picture of the star formation in host galaxies (see also Alaghband-Zadeh et al. 2016).

In this paper, we try to overcome some of the limitations described above. We will characterize spatially resolved properties of the Hα emission in a large sample of moderate to high-luminosity AGN at z $\sim$ 2 (Log $L_{\rm bol}$ = 45.4–47.9 erg s^{-1}). These AGN show the presence of high velocity ionized gas outflows in their host galaxies, which was inferred from the [O III]λ5007 emission (Kakkad et al. 2020). We investigate whether the Hα emission is dominated by star formation or AGN ionization. In the case where the Hα emission is dominated by AGN ionization, we will determine whether this emission is also a part of ionized gas outflows in the narrow line region (NLR). Finally, using the spatially resolved Hα and [O III]λ5007 emission ([O III], hereafter), we investigate whether the outflows and star formation are colocated and whether this can reveal the presence of positive or negative feedback in these galaxies.

We adopt the following ΛCDM parameters throughout this paper: $H_{\rm o}$ = 70 km s^{-1}, $\Omega_{\rm M}$ = 0.3 and Ω_{Λ} = 0.7. In all the maps in this paper, North is up and East is to left.

2 SAMPLE, OBSERVATIONS, AND DATA REDUCTION

The sample in this study is part of the SINFONI survey for Unveiling the Physics and Effect of Radiative feedback (see Circosta et al. 2018; Kakkad et al. 2020; Mainieri et al. 2021). SUPER is an ESO large programme with the SINFONI instrument on board the VLT (Eisenhauer et al. 2003) designed to characterize the properties of outflows in the ionized gas phase and their impact on host galaxies in a sample of 39 X-ray selected AGN at z ∼ 2 in AGN host galaxies at z ∼ 2. The survey is designed to trace ionized gas kinematics in the least biased manner by probing a wide range in AGN bolometric luminosity that span up to four orders of magnitude. The survey takes advantage of the adaptive optics (AO) module and reaches an angular resolution of ∼0.2 arcsec, resolving ionized gas kinematics and potentially star formation down to ∼2 kpc scales. Here, we provide a brief description of the sample chosen for this paper and refer the reader to Circosta et al. (2018) and Vietri et al. (2020) for more details about the parent sample.

The 39 X-ray selected AGN ($L_{2\text{-}10\text{keV}} > 10^{42}$ erg s^{-1}) were obtained from shallow and deep fields: *Chandra* Deep Field South (e.g. Luo et al. 2017), COSMOS-Legacy (e.g. Civano et al. 2016), XMM-XXL (e..g, Georgakakis & Nandra 2011; Liu et al. 2016; Menzel et al. 2016), Stripe 82 X-ray survey (e.g. LaMassa et al. 2016) and *WISE*/SDSS selected Hyper-luminous quasar sample (e.g. Bischetti et al. 2017; Vietri et al. 2018). Out of these 39 AGN, 22 are classified as type 1 (56 per cent) based on the presence of broad H β, H α, and/or Mg II lines, characteristic of emission from the Broad Line Region (BLR). A wide range of ancillary data has allowed us to accurately compute various AGN properties such as the AGN bolometric luminosity ($L_{\rm bol}$), the black hole mass ($M_{\rm BH}$), X-ray column density ($N_{\rm H}$) in most targets and host properties such as SFR and stellar mass (M_*) in type 2 AGN. Estimation of host galaxy properties in type 1 AGN has been challenging as the AGN emission dominates the spectral energy distribution (SED) for a wide range of wavelengths, preventing a robust estimation of SFR and stellar mass. Furthermore, CO(3-2) and dust continuum follow-up using sub-mm data from ALMA has also provided constraints on the molecular gas and dust properties for a sub-sample of SUPER targets (Circosta et al. 2021; Lamperti et al. 2021).

The SINFONI observations for the SUPER survey were carried out in the H-band and K-band (or the $H + K$ band in the case of bad weather) to trace the rest-frame optical emission lines: H β, [O III]λ4959, 5007, [N II]λ6549, 6585, H α, and [S II]λλ6716, 6731. The spatial resolution of the Adaptive Optics-assisted observations in the *K*-band grating reaches down to 0.2 arcsec (median 0.3 arcsec), similar to the *H*-band data, which corresponds to a physical scale of ∼2 kpc at z ∼ 2. The $H + K$ grating observations have a spatial resolution of ∼0.9 arcsec(∼7.5 kpc) and did not have sufficient offset along the X-direction while nodding during the observations. This implied that a spatially resolved analysis was only performed along the Y direction. Further details about the observations, data reduction, and results from the [O III] analysis of the *H*-band data of type 1 SUPER targets are available in the first SINFONI data release paper (Kakkad et al. 2020). This paper focuses on the analysis of the H α emission line in the 21 type 1 SUPER targets, observed with the *K*-band or $H + K$ band grating of the SINFONI spectrograph. We focus on the type 1 AGN to have a better estimate of PSF smearing effects by modelling the emission from the BLR. We have excluded the type 1 AGN S82X2106, since no signal was detected in our *K*-band observations. The targets in this paper have the following ranges in their black hole and host galaxy properties: log $M_*/{\rm M}_\odot$ ∼ 10.38–11.20, SFR <94–686 M$_\odot$ yr^{-1}, log $L_{\rm bol}$/[erg s^{-1}] ∼ 45.4–47.9, log $M_{\rm BH}/{\rm M}_\odot$ ∼ 8.3–10.7, and log $N_{\rm H}$/cm^2 ∼ <21.25–24.1. Tables with full list of these values for each target are available in Circosta et al. (2018), Kakkad et al. (2020), and Vietri et al. (2020).

3 ANALYSIS

One of the primary goals of this paper is to investigate whether the observed H α emission is ionized by star formation or the AGN. We also compare the H α morphology and kinematics from the *K*-band data with that of the [O III] line presented in Kakkad et al. (2020) to infer if the ionized gas outflows have an impact on the unobscured star formation.

In Kakkad et al. (2020), we characterized the properties of the ionized gas kinematics in the NLR of the type 1 AGN from the SUPER sample using the [O III]λ5007 line in the *H*-band data. We describe the main results from the *H*-band data briefly here before presenting the analysis methods used in this paper. The non-parametric [O III] velocity dispersion, w_{80}, of the SUPER sample was always above 600 km s^{-1}, a velocity-cut usually indicative of the presence of ionized gas outflows driven by the AGN. The AGN as a source of outflow was also confirmed by the presence of strong correlations between the different ionized gas outflow properties (w_{80}, maximum velocity, $v_{\rm max}$, and mass outflow rates) and the AGN properties [$L_{\rm X}$(2-10 keV), $L_{\rm bol}$, $M_{\rm BH}$ and $\lambda_{\rm Edd}$]. The ionized gas emission is extended in seven out of 11 targets for which the signal to noise in the [O III] emission was sufficient enough to perform a PSF deconvolution. The outflows associated with the ionized gas is extended up to ∼6 kpc from the AGN location, although <10 per cent of these outflows have the potential to escape the gravitational pull of the host galaxy.

3.1 Modelling of the integrated spectrum

We first construct a model for the integrated spectrum before performing a pixel-by-pixel analysis of the emission lines in the *K*-band data. We extract the integrated spectrum for each object using a circular aperture centred on the AGN. The peak of the *K*-band continuum emission is used as an estimate for the AGN location and the aperture size was chosen to include at least ∼95 per cent of the total emission. We used the spectrum extracted from an object-free region to estimate the error on the spectrum. We focused the modelling of the extracted spectrum around the H α and [S II] emission line regions.

Modelling the H α emission line profiles of high-redshift type 1 AGN host galaxies is not straightforward as the [N II] and H α emission lines are blended into one broad feature. Each emission line is modelled using multiple Gaussian functions. The H α emission consists of contributions from clouds from the BLR, NLR, and emission from the host galaxy. The NLR component(s) of [N II]λ6549, 6585 emission (as well as [S II]λ6716, 6731) can be blended with the different components of the H α emission. As a result of such complex nature of the emission around the H α line (referred to as the H α complex hereafter), there is no unique solution to the emission line model. Therefore, constraints need to be imposed on different Gaussian parameters in order to obtain a unique solution. In this section, we explore the different ways of fitting the H α complex in the type 1 AGN host galaxies, based on methods previously adopted in the literature. We will then present the arguments that justify the fitting methodology adopted in this paper.

We model the H α complex using three fitting methods, which we will call M1, M2, and M3. The three methods differ on

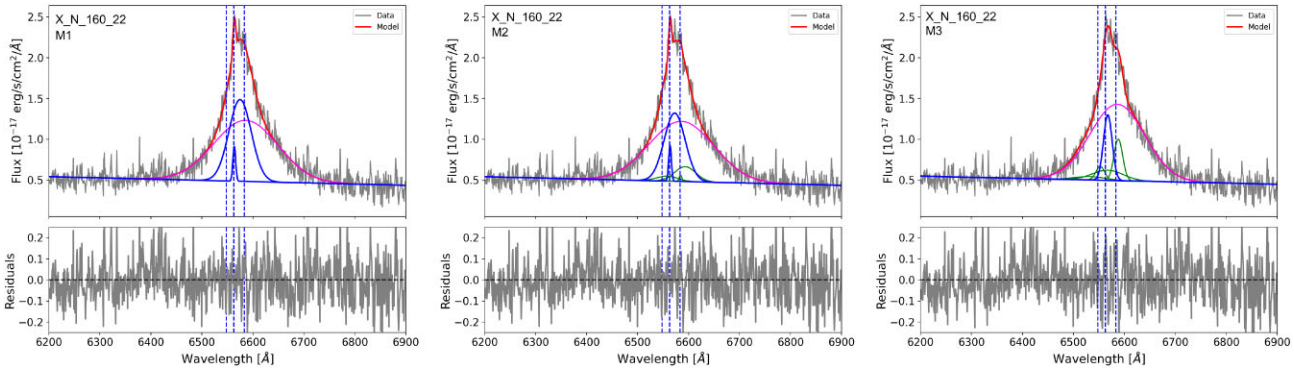

Figure 1. The top panel shows the integrated spectrum of X_N_160_22 extracted from a circular aperture of 0.9 arcsec diameter, showing the Hα complex i.e. [N II]$\lambda\lambda$6549,6585 and Hα lines blended together. The left-hand panel shows the line fitting model M1, the middle panel M2 and the right-hand panel M3. The bottom panels show the residuals from the emission line modelling. Further details on the three models are described in Section 3.1. The figure highlights the differences in the Gaussian models when imposing different constraints on the fitting routines and that the Hα complex modelling is often degenerate. In all the panels, the grey curve shows the raw spectrum extracted from the cube (or the residuals in the bottom panel), the red curve shows the overall model, the blue curves show the Hα NLR models, the magenta curve represents the Hα BLR emission, and the green curve shows the [N II]$\lambda\lambda$6549,6585 emission. The *x*-axis shows the rest-frame wavelength and the *y*-axis shows the observed flux. The vertical dashed blue lines show the expected location of [N II]$\lambda\lambda$6549,6585 and Hα lines based on the redshift of this target. The [S II]$\lambda\lambda$6716, 6731 lines remain undetected in most galaxies.

some of the constraints imposed on the emission lines within the Hα complex. These constraints are based on the results of the Hβ and [O III] emission line models presented in Kakkad et al. (2020). We start describing the assumptions common to the three methods used to model the Hα complex. The integrated spectrum is modelled between the rest-frame wavelengths 6200–6900 Å which includes the AGN continuum emission, [N II]$\lambda\lambda$6549,6585, Hα, and [S II]$\lambda\lambda$6716,6731 emission lines. The BLR component of Hα is modelled using a broad Gaussian or a broken power law, the choice depending on the model used to reproduce the Hβ line in the *H*-band data (see also Vietri et al. 2020). The NLR components of Hα and [N II]λ6549, 6585 are modelled using multiple Gaussian functions. A maximum of two Gaussians were used to reproduce the non-BLR components of each emission line ([N II]λ6549, 6585 and Hα), equal to the number used for the [O III] line. In the case when two Gaussians are used for the NLR component, the Gaussian with the lower width is labelled as the narrow component, while the one with larger width is labelled as the broad component, without setting strict lower or upper limits for each component. To distinguish between the broad Gaussian component from the NLR and the one from the BLR, we will use the term broad Gaussian for the former and BLR-Gaussian for the latter. The widths of the narrow (broad) Gaussian components of [N II] and Hα are coupled to each other and the centroid difference between each component is fixed based on the expected positions in the rest-frame spectra. Furthermore, the relative ratio between the fluxes of [N II]λ6549 and [N II]λ6585 is fixed to the expected theoretical value of 1:3 (e.g. Osterbrock & Ferland 2006). We do not include fitting models for an iron component or [S II]$\lambda\lambda$6716,6731, as they remain undetected or their contribution is negligible in all the galaxies.

We now describe the differences in the fitting constraints between the three methods. In the M1 method, we first fit the Hα complex using only the Hα components. The [N II] line components are added only when the models from the Hα only fit result in significant residuals on visual inspection. This approach was previously adopted in the literature for the analysis of the rest-frame optical spectra of one of the high-z quasars (e.g. Carniani et al. 2016), where the [N II] emission is assumed to be undetected if no significant residuals are present after modelling with only the Hα components. In the M2 method, [N II] emission line model is included, irrespective of the presence or absence of residuals from the Hα-only fit. The M2 method assumes that the [N II] emission is always present within the Hα complex. Similar to the M1 method, no other constraints from the *H*-band spectra are imposed apart from the common constraints described in the previous paragraph. The M2 method is explored to gauge the variation in the fluxes and widths of various Hα components upon inclusion of the [N II] lines. Lastly, in the M3 method, we fit the [N II] line in the Hα complex, similar to the M2 method. However, three additional constraints are imposed during the line fitting procedure: (1) The maximum allowed width of the narrow Hα component is the width of the narrow [O III] line from the *H*-band line fitting results. (2) The difference in the centroid of narrow and broad Gaussian components of Hα is kept the same as the difference in the centroid of narrow and broad Gaussian components of the [O III] line. (3) The width of the broad Hα component is kept the same as that of the broad [O III] components. The method M3 is similar to the fitting model presented in Vietri et al. (2020), with the exception that [S II]$\lambda\lambda$6716,6731 emission line components were not included. Fig. 1 shows the integrated spectrum and the emission line modelling of X_N_160_22 as an example, using the three methods (left-hand panel: M1, middle panel: M2, and right-hand panel: M3). The integrated spectra of the rest of the targets are shown in the Appendix A (Figs A1 and A2). Below, we present arguments to support the selection of the M3 method as our baseline methodology in this paper.

Tables 1, A1, and A2 report the fitting parameter values obtained using the three methods described above (M3, M2, and M1, respectively). In most of the type 1 AGN, the [N II] emission is required as significant residuals remain from the Hα-only fitting procedure. Therefore, in the cases where such residuals are not observed from the Hα-only fit, we assume that the [N II] lines are actually blended with the overall emission line structure. The presence of [N II] lines in most high-redshift galaxies is also supported by the results of the SINS/zC-SINF survey (e.g. Förster Schreiber et al. 2018) where ∼65 per cent of the star forming galaxies had [N II] detections. However, the M2 method returns very high values for the width of the BLR component of the Hα line (>9000 km s^{-1} in some cases), which would result in unrealistically high black hole masses. This is a direct consequence

Table 1. This table reports the H α emission line fitting parameters using the M3 model described in Section 3.1 (see also Vietri et al. 2020) and whether the emission is extended. (1) Target name, (2) The diameter of the circular aperture used for spectral extraction, Columns (3) and (4) report the width (FWHM) of the individual NLR Gaussian components of the H α line (narrow NLR = v_1 and broad NLR = v_2), (5) width (FWHM) of the BLR Gaussian component of H α. Columns (6), (7), and (8) report the luminosity of the two NLR components (narrow NLR = L_1 and broad NLR = L_2) and the BLR component (L_{BLR}), respectively, (9) reports the presence or absence of extended H α emission. The errors are obtained using a Monte Carlo approach and the values reported are the 1σ error limits. *Targets with the same line fitting results as the M2 model (Table A1). Line modelling for all the targets has been done between rest-frame wavelengths 6200–6900 Å, except J1441+0454 for which the fitting is performed between rest-frame wavelengths 6380–6950 Å.

Target	Aperture	FWHM			$L_{H\alpha}$			Extended H α
		v_1	v_2	v_{BLR}	L_1	L_2	L_{BLR}	
	arcsec	km s^{-1}	km s^{-1}	km s^{-1}	erg s^{-1}	erg s^{-1}	erg s^{-1}	
(1)	(2)	(3)	(4)	(5)	(6)	(7)	(8)	
X_N_160_22	0.9	915 ± 195	–	5730 ± 156	43.44 ± 0.78	–	44.30 ± 0.03	Yes
X_N_81_44	0.9	530 ± 162	2000 ± 213	6621 ± 324	42.82 ± 0.19	43.72 ± 0.12	44.26 ± 0.02	Yes
X_N_53_3*	0.8	345 ± 213	–	4577 ± 187	42.04 ± 0.22	–	43.70 ± 0.01	Yes
X_N_66_23*	0.9	150 ± 150	–	5640 ± 190	41.45 ± 7.8	–	43.72 ± 0.01	May be
X_N_35_20*	0.5	532 ± 56	–	6549 ± 1188	41.97 ± 0.08	–	42.68 ± 0.08	No
X_N_12_26*	1.0	544 ± 42	–	4615 ± 99	42.80 ± 0.04	–	43.95 ± 0.01	Yes
X_N_44_64*	0.5	411 ± 17	–	7688 ± 560	42.37 ± 0.02	–	43.03 ± 0.02	No
X_N_4_48*	0.7	473 ± 53	–	7596 ± 303	42.79 ± 0.06	–	44.18 ± 0.01	Yes
X_N_102_35	0.3	–	1735 ± 480	5418 ± 246	–	42.93 ± 0.24	43.94 ± 0.03	No
X_N_115_23	0.9	413 ± 55	1400 ± 267	7031 ± 148	42.93 ± 0.08	43.25 ± 0.09	44.15 ± 0.01	Yes
cid_166	0.9	395 ± 126	1875 ± 226	6881 ± 104	42.48 ± 0.27	43.76 ± 0.11	44.60 ± 0.01	May be
cid_1605*	0.3	516 ± 110	–	3802 ± 80	41.96 ± 0.15	–	43.27 ± 0.01	Yes
cid_346*	0.9	301 ± 43	2916 ± 156	7556 ± 592	42.60 ± 0.08	43.59 ± 0.16	43.86 ± 0.05	Yes
cid_1205*	0.8	446 ± 89	–	5023 ± 183	42.04 ± 0.12	–	43.46 ± 0.01	No
cid_467*	0.3	575 ± 61	–	8750 ± 285	42.37 ± 0.05	–	43.86 ± 0.01	Yes
J1333+1649	1.0	615 ± 572	2760 ± 771	6217 ± 467	42.77 ± 0.67	44.74 ± 1.28	45.53 ± 0.02	Yes
J1441+0454	1.0	–	1000 ± 85	5262 ± 90	–	44.18 ± 0.03	44.92 ± 0.02	No
J1549+1245	1.1	376 ± 221	1385 ± 298	7914 ± 97	43.40 ± 0.30	44.36 ± 0.20	45.63 ± 0.01	May be
S82X1905	1.0	660 ± 58	–	4935 ± 99	43.01 ± 0.04	–	44.12 ± 0.01	Yes
S82X1940	0.8	380 ± 124	1428 ± 710	4145 ± 434	42.76 ± 0.25	42.80 ± 4.53	44.25 ± 0.11	Yes
S82X2058	0.9	363 ± 128	1675 ± 228	6616 ± 184	42.13 ± 0.30	42.56 ± 3.06	44.09 ± 0.02	Yes

of leaving all the emission line component centroids and widths free to vary. The presence of unrealistic widths and degeneracy in the results are solved using the M3 method. Therefore, hereafter, we will use the M3 method in this paper to model the H α complex, which is also similar to the methodology adopted in previous papers from the SUPER survey (e.g. Vietri et al. 2020; Lamperti et al. 2021).

We employ a Monte Carlo (MC) approach to determine the errors in the fitting model, where we add noise to the integrated model and repeat the fitting procedure 100 times to determine the 1σ errors on different parameters (see e.g. Perna et al. 2015; Brusa et al. 2016; Kakkad et al. 2016). The input noise for the MC is determined from the rms noise in an emission line-free region in the raw spectrum.

3.2 Extended H α emission

Before performing a pixel-by-pixel analysis of the H α spectrum of the type 1 targets, it is important to quantify the contribution of beam-smearing from the AGN PSF to the observed H α emission. This procedure, also called PSF-subtraction, isolates the underlying contributions from the host galaxy. Beam smearing results in emission line regions to mimic radial profiles consistent with PSF profiles, and consequently appear artificially extended (see e.g. Carniani et al. 2015; Husemann et al. 2016; Luo et al. 2019). We subtract this contribution from the AGN-PSF using methods similar to those employed in the analysis of the extended [O III] emission in the *H*-band data in Kakkad et al. (2020).

If the H α emission is unresolved, then the spectrum at any distance from the AGN will be the same as the spectrum at the AGN location, except for an overall scaling factor across the spectrum (e.g. Jahnke et al. 2004). Therefore, we first model the spectrum extracted at the AGN location (circular aperture of diameter 0. 1 arcsec centred on the *K*-band continuum peak). We will refer to this spectrum as the 'nuclear model'. The nuclear model is subtracted from every pixel across the SINFONI field-of-view, only allowing a variation in the overall normalization factor of the spectrum. The kinematic parameters of different Gaussian components (i.e. the line centroid and the line width) are kept fixed with respect to the nuclear model. After the subtraction of the PSF model, we collapsed the channels in the residual data cube at the expected location of narrow H α emission. The width of the channel window is optimized for each target separately, based on where we obtain the maximum residual H α emission. A noisy map (an image with net zero residuals) indicates that the underlying H α emission is unresolved, while systematic patterns in these residual maps would suggest that the H α emission is extended. This extended H α emission can be due to star formation in the host galaxy, AGN emission, or a combination of the two. The nature and origin of this extended emission will be discussed further in Section 3.3.

Figs 2 and 3 show the results of the PSF-subtraction method for each target presented in this paper. We do not show the PSF-subtraction results for the following four targets: X_N_35_20, X_N_44_64, X_N_102_35 and J1441+0454. Targets X_N_35_20 and X_N_44_64 had low S/N in their H α line in the integrated spectrum to obtain a reliable estimate on the H α BLR flux and consequently the PSF. X_N_102_35 was observed in the $H + K$ band and no residuals were observed in the Y-direction. Lastly, the location of the H α line in J1441+0454 is contaminated by telluric emission and the PSF-subtraction did not yield a reliable detection.

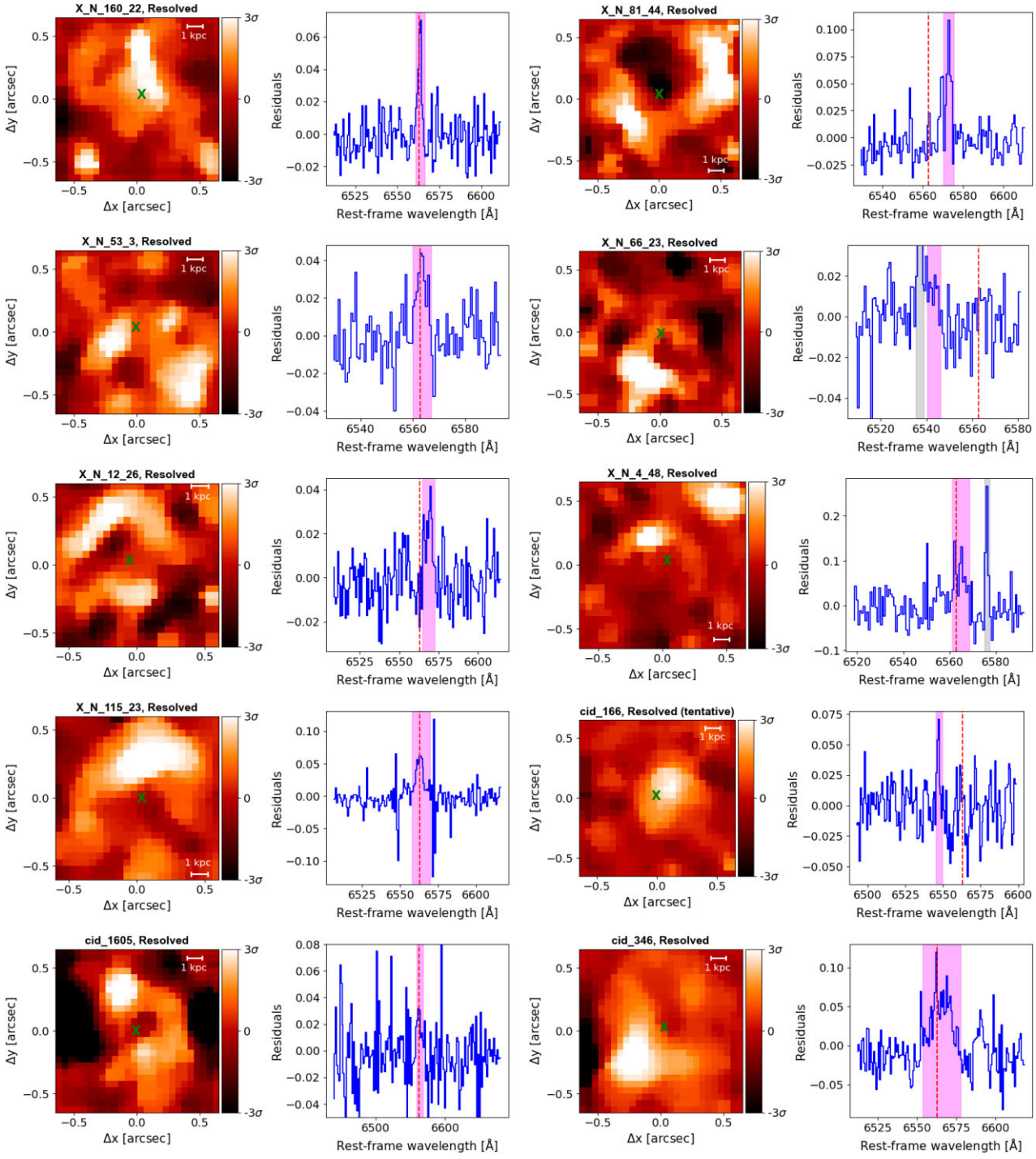

Figure 2. The plots in this figure show the results of the PSF-subtraction procedure described in Section 3.2. The maps show the PSF-subtracted Hα channel map and the corresponding right-hand panels show the spectrum extracted from regions above 3σ noise levels (white regions in the channel maps). The noise levels in each map is obtained from object-free regions. The 'X' in the maps mark the peak of the *K*-band continuum emission which is used as a proxy for the AGN location. The magenta shaded region in the spectra show the channels that were collapsed to obtain the PSF-subtracted images. The vertical red dashed line shows the expected location of the Hα line based on the redshift of the respective targets. The presence of structure in the PSF-subtracted map and a visible detection of the emission line in the spectra would suggest an extended Hα feature. Each target in this figure shows signatures of extended Hα emission (labelled as 'Resolved'), except X_N_66_23 and cid_166 (labelled as 'Resolved?') where the extension is a possibility but unconfirmed with the current data. Further details are given in Section 3.2.

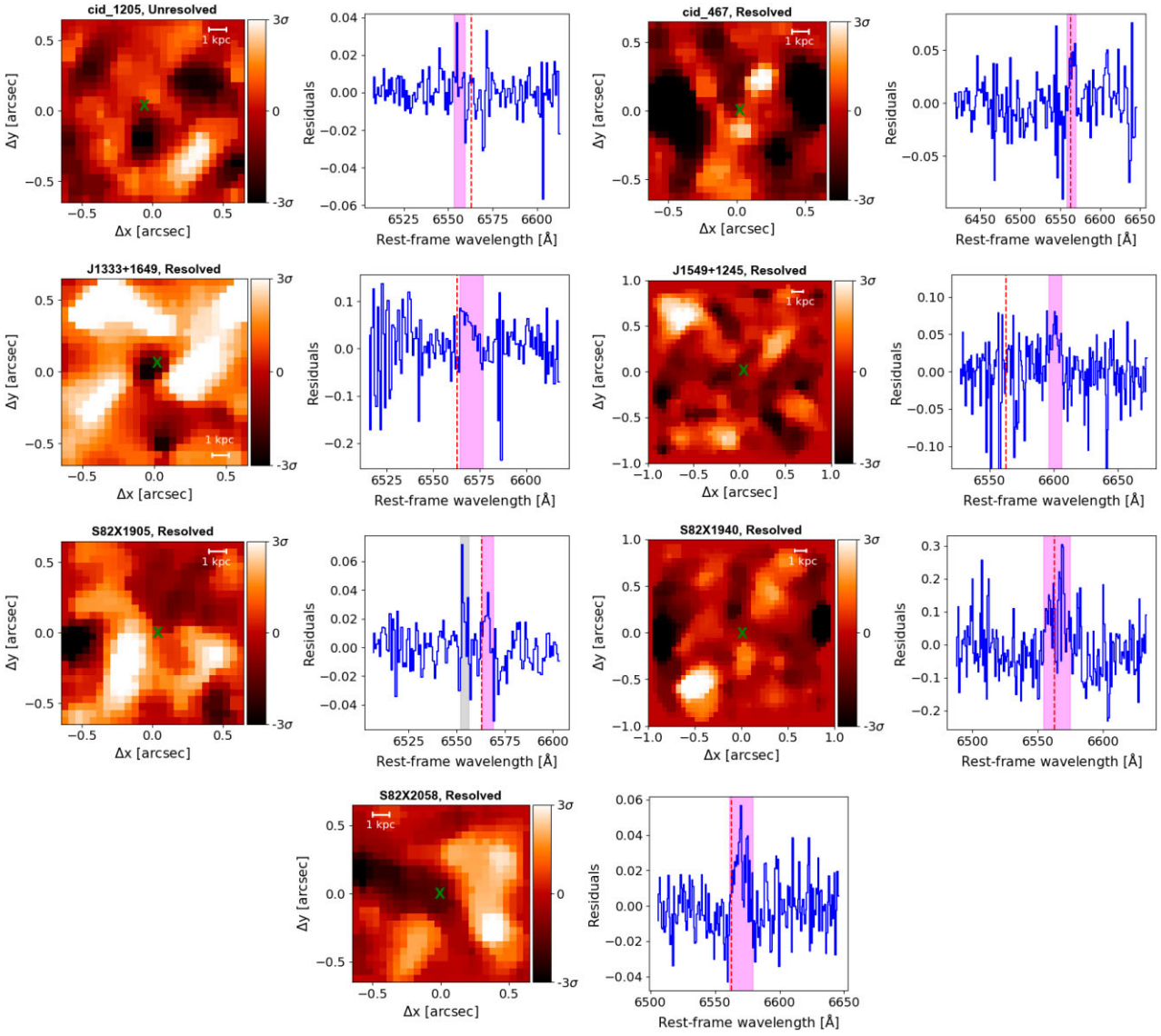

Figure 3. Same as Fig. 2, for the rest of the targets presented in this paper. All the targets, except cid_1205 and J1549+1245, show confirmed evidence of extended H α emission. We detected no extended emission in cid_1205 and the detection in J1549+1245 is tentative.

All the maps in Figs 2 and 3 show the PSF-subtracted channel maps at the expected location of H α emission. The colour map in the H α images is set between ±3σ, where σ is the noise level in the map determined from object-free locations. The panels on the right side of the maps show the spectrum extracted from regions at or above 3σ in the H α channel maps. The magenta shaded regions in the spectra show the channels that were collapsed to obtain the PSF-subtracted H α map. The vertical dotted red line in the spectra shows the expected location of the H α line based on the [O III] redshift values reported in Kakkad et al. (2020).

We confirm the presence of extended H α emission in 13 out of the 21 galaxies and three galaxies (X_N_66_23, cid_166 and J1549+1245) show tentative evidence of extended emission. The detection in X_N_66_23 is classified as a tentative one, as the extended emission is observed at a blue-shift of ∼1200 km s^{-1} from the expected location of the H α line in the spectra. Similarly, the extended emission in J1549+1245 is detected at a distance of 9 kpc from the AGN location and the spectral position of the detection is redshifted by ∼+1800 km s^{-1} with respect to the expected location of the H α line. Although currently available archival optical observations do not suggest the presence of companions, this may be due to their limited spatial resolution. In fact, ALMA CO observations of J1549+1245 have shown the presence of a possible companion south of the AGN location (see Bischetti et al. 2021). Such extreme velocity shifts have been observed in previous CO observations of high redshift X-ray AGN sources (e.g. Carniani et al. 2017). The extended H α detections in X_N_66_23 and J1549+1245 may suggest emission from tidal tails. In the case of cid_166, the detection is almost at the limit of the spectral resolution of SINFONI. Furthermore, the observed residual is blue-shifted by ∼700 km s^{-1} from the expected location of the H α emission and therefore the extended emission in cid_166 has been classified as a tentative detection. cid_1205 is the only target among the ones observed with AO and with sufficient S/N for the PSF-subtraction analysis that shows no extended H α emission.

Overall, we find a higher fraction of targets with extended H α emission (∼76 per cent including the tentative detections) than extended [O III] emission (∼35 per cent). The spatial extent of the H α

Table 2. Properties of the extended H α emission presented in this paper. (1) Target name, (2) The maximum distance from the AGN location where the extended H α is detected at $\geq 3\sigma$ after the PSF subtraction (see Figs 2 and 3), (3) The width of the PSF-subtracted H α emission line from the extended regions, (4) The extended H α centroid in the spectral space with respect to the expected location of H α based on the [O III] redshift from Kakkad et al. (2020), (5) The flux ratio, [N II]/H α from the extended H α spectra from the *K*-band data, (6) The flux ratio [O III]/H β from the extended [O III] spectra from the H-band data (Kakkad et al. 2020), (7) The ionization source of the extended H α emission line regions based on its location in the BPT diagram or the [N II]/H α flux ratio. Further details in Section 3.3. This table does not show the data for X_N_35_20, X_N_44_64, X_N_102_35, cid_1205, cid_467, and J1441+0454, as these targets are unresolved.

Target	$R_{H\alpha}$ kpc	$v_{H\alpha}$ km s^{-1}	v_{shift} km s^{-1}	log [N II]/H α	log [O III]/H β	Ionization source
(1)	(2)	(3)	(4)	(5)	(6)	(7)
X_N_160_22	4.5 ± 0.4	112 ± 30	42 ± 10	<-0.7	–	SF
X_N_81_44	3.5 ± 0.4	113 ± 15	485 ± 5	<-0.8	–	SF
X_N_53_3	5.2 ± 0.4	199 ± 44	33 ± 17	$-0.6^{+0.2}_{-0.4}$	–	unconstrained
X_N_66_23	4.0 ± 0.4	370 ± 109	−1200 ± 300	<-0.9	–	SF
X_N_12_26	4.5 ± 0.4	241 ± 45	286 ± 21	<-0.6	–	unconstrained
X_N_4_48	6.4 ± 0.4	256 ± 58	78 ± 29	<-0.4	–	unconstrained
X_N_115_23	4.6 ± 0.4	270 ± 35	19 ± 15	<-0.8	0.9 ± 0.3	AGN
cid_166	2.6 ± 0.4	73 ± 16	−713 ± 9	<-0.5	–	unconstrained
cid_1605	3.9 ± 0.4	351 ± 140	10 ± 1	<-0.3	–	unconstrained
cid_346	4.7 ± 0.4	628 ± 45	134 ± 20	<-0.4	>0.5	AGN
cid_467	2.6 ± 0.4	350 ± 65	180 ± 25	<-0.7	–	SF
J1333+1649	5.7 ± 0.4	302 ± 67	260 ± 22	<-0.5	0.7 ± 0.2	AGN
J1549+1245	9.0 ± 0.4	408 ± 92	1720 ± 200	<-0.4	–	unconstrained
S82X1905	4.4 ± 0.4	142 ± 28	143 ± 12	<-0.6	>1.0	AGN
S82X1940	7.8 ± 0.4	784 ± 98	202 ± 120	<-0.2	–	AGN
S82X2058	4.4 ± 0.4	436 ± 68	330 ± 30	<-0.4	–	unconstrained

emission (maximum distance between the AGN location and the H α emission in the PSF-subtracted maps), $R_{H\alpha}$ is in the range 3–9 kpc, with a mean value of ∼5 kpc. Due to the low signal to noise after the PSF-subtraction, we model the extended H α residual spectrum using single Gaussian functions and define two parameters: the width (FWHM) of the extended H α emission, $FWHM_{H\alpha}$, and the velocity shift, v_{shift}, between the expected location of the H α line and actual location of the extended H α line in the spectra. We find $FWHM_{H\alpha}$ in the range 73–784 km s^{-1} with a mean width of 312 km s^{-1}. The velocity shift, v_{shift} is in the range −1200–1720 km s^{-1}, with the majority of the targets showing redshifted H α emission. Only two targets, X_N_66_23 and cid_166, display blue-shifted extended H α emission and both of these targets are classified as having a tentative extended emission. The properties of the extended H α emission are summarized in Table 2.

We investigated whether the properties of the extended H α emission, namely $R_{H\alpha}$, $FWHM_{H\alpha}$, and v_{shift} show any correlations with the AGN or host galaxy properties such as L_{bol}, M_{BH}, SFR, and M_*. We derived the Pearson coefficient and the p-value (null hypothesis probability for non-correlation) for the individual relations. The p-values for different correlations are summarized in Fig. 4. We define a correlation to exist based on $p < 0.05$. Accounting for the errors, v_{shift} correlates with M_{BH} and possibly also with L_{bol}, and SFR. R_{kpc} also shows correlation with M_* and possibly with L_{bol}. No correlations are found between $FWHM_{H\alpha}$ and the AGN or host galaxy properties. However, we note that since these are type 1 targets, the host galaxy properties, namely SFR and M_*, are highly unconstrained and are only available for five targets (see Circosta et al. 2018). Overall, the v_{shift} parameter seems to correlate strongly with the AGN properties suggesting that the observed velocity shift is possibly due to outflowing ionized gas traced with H α. On the other hand, the size of the extended region correlates with the galaxy mass, consistent with the correlations reported between the size and stellar mass of galaxies (e.g. van der Wel et al. 2014). Furthermore,

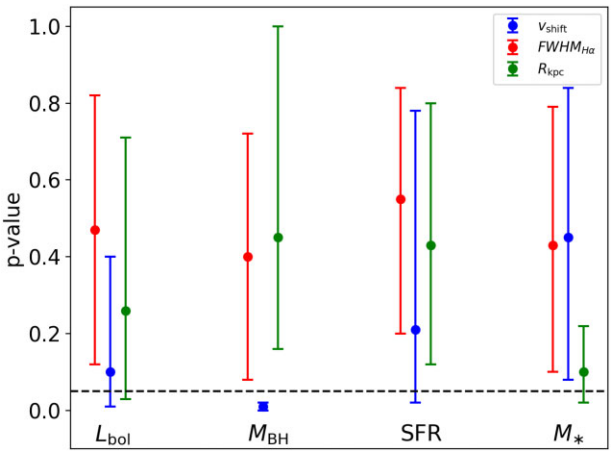

Figure 4. The plot shows the null-hypothesis probability for non-correlation between different extended H α properties and the properties of the black hole and the host galaxy. The dashed black line shows the 5 per cent line for p-value, used as a demarcation between the presence or absence of correlations.

the lack of correlations or weaker correlations in Fig. 4 may also suggest that the observed H α emission in some galaxies might also be tracing a companion galaxy i.e. not associated with the X-ray source or the host galaxy itself. The presence of companions will be further discussed in Section 4.

3.3 Ionization source of the extended H α emission

We now discuss the ionization source of the extended H α emission, i.e. whether the emission is ionized by the AGN, star formation, or a combination of the two, based on the [O III] results reported in Kakkad et al. (2020) and PSF-subtracted images and spectra shown in

Figs 2 and 3. We use three different techniques to infer the ionization source: (1) We compare the extended H α morphology with the [O III]morphology. A similarity between the two emission regions could suggest that the extended H α emission traces gas in the NLR. (2) As described in Section 3.2, we fit the single Gaussian functions to the extended H α emission to derive the line width. A large width (e.g. $>600\,\mathrm{km\,s^{-1}}$) would mean H α emission traces outflowing gas. This is supported by the maximum gas velocity of $\sim500\,\mathrm{km\,s^{-1}}$ observed in the case of star formation driven outflows in high-redshift galaxies (see review by Förster Schreiber & Wuyts 2020), and therefore using $600\,\mathrm{km\,s^{-1}}$ as a cut off for AGN-driven outflows is a conservative assumption. However, we note that galaxy interactions can also increase the line widths (e.g. Puglisi et al. 2021). Due to the relatively low S/N of the H α lines compared to integrated spectra, we do not attempt to fit multiple Gaussian functions to these spectra. (3) Lastly, the single Gaussian fits to the extended H α emission (Section 3.2, Fig. 2) were used to estimate the flux of the [N II]and H α lines. The flux ratios were then placed on the classical Baldwin, Phillips & Telervich (BPT; see Baldwin, Phillips & Terlevich 1981; Veilleux & Osterbrock 1987) diagnostic diagrams to estimate the probable source of ionization from expectations based on the literature (e.g. Kauffmann et al. 2003). For the majority of the galaxies, extended [O III] and H β emission lines are not detected at the location of extended H α emission, therefore placing them on the BPT diagrams was not possible.

We were able to plot resolved BPT maps for four galaxies, namely X_N_115_23, cid_346, J1333+1649, and S82X1905, as extended [O III] emission is also detected at the location of extended H α as shown in the top two rows of Fig. 5. The bottom panel in Fig. 5 shows the location of extended emission in these four galaxies in the [N II]-BPT diagram. In these four galaxies, the spatial coincidence of the extended H α and [O III] emission suggests that we are tracing the NLR rather than the host galaxy disc. That the ionization source for the extended H α is the AGN rather than star-formation is further supported by the location of these galaxies in the BPT diagram (bottom panel in Fig. 5). The [N II] line remains undetected in the extended H α region for all the galaxies and therefore we estimate an upper limit for the [N II]/H α ratio. In the case of cid_346 and S82X1905, we also do not detect H β emission in the extended regions and therefore a lower limit to the [O III]/H β line ratio is estimated. All four galaxies are above the region of the BPT, where we expect to have star formation as the main ionization source. In addition, for cid_346, the width of the extended H α emission is $628 \pm 45\,\mathrm{km\,s^{-1}}$, which is above the limit usually used to distinguish between an outflowing and non-outflowing gas. This suggests that the observed H α emission is a part of the NLR outflow. This is also supported by the fact that the ionized outflow is also detected in the [O III] line at the same location as the extended H α (see Kakkad et al. 2020). We also note here that the BPT results shown here for cid_346 may be different compared to the ones presented in Lamperti et al. (2021), as the extraction apertures for the PSF and the extended H α emission may be different.

For all the other galaxies, as the [O III]and H β lines remain undetected, they could not be placed in the classical BPT diagram. Therefore, we estimate the ionization source based on the limit derived for the [N II]/H α line. Four targets, X_N_160_22, X_N_81_44, X_N_66_23, and cid_467, have log([N II]/H α) values <-0.7 and with such low [N II]/H α line ratios, it is less likely for these sources to be ionized by the AGN (see the results from low redshift galaxy sample in Kauffmann et al. 2003). For one of them, X_N_81_44, we also have evidence that the [O III] and H α emission are extended, but are not spatially colocated (Fig. 6, left-hand panel). We would

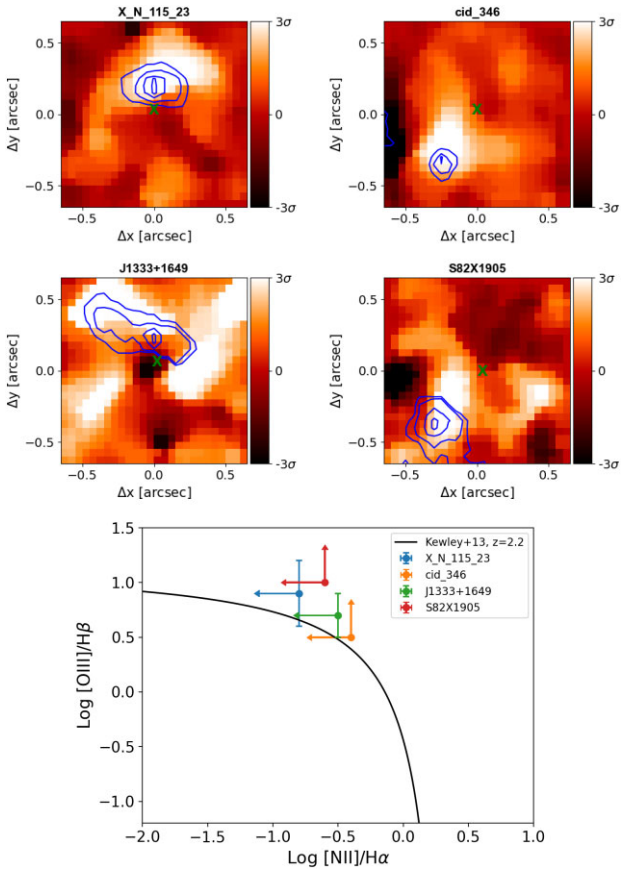

Figure 5. The background images in the maps in the top two rows shows the PSF-subtracted H α images and the overlaid blue contours show the locations of extended [O III] emission. The contour levels are at 98, 90, 70, and 50 per cent of the peak [O III] flux. In four targets, X_N_115_23, cid_346, J1333+1649, and S82X1905, the spatial location of the extended H α emission coincides with that of the [O III] emission. This made it possible to place the extended H α emission of these four galaxies in the BPT diagram shown in the bottom panel. In all these four galaxies, the extended emission is ionized by the AGN. The black line shows the division between star forming and AGN ionization from Kewley et al. (2013). Targets, X_N_81_44 and J1549+1245 do not show the same location of the [O III] and H α emission.

therefore classify the extended emission in these four galaxies as most probably ionized by starformation.

The galaxies where the log ([N II]/H α) line ratio >-0.7, the source of ionization could not be constrained for the extended regions with the current data. The target, J1549+1245 falls under this category, where the extended [O III] and H α emission are not spatially colocated (Fig. 6, right-hand panel). Therefore, the ionization sources of these targets are labelled as 'unconstrained' in Table 2. An exception is S82X1940 shows an extended H α emission towards the SE direction from the AGN location (Fig. 3). This target displays the largest H α line width in the extended region of $\sim784 \pm 98\,\mathrm{km\,s^{-1}}$. The [O III] emission line analysis of this target already shows the presence of an ionized outflow (Kakkad et al. 2020) and therefore the H α emission most likely also traces the outflowing gas driven by the AGN. Based on this evidence, we conclude that the observed extended H α emission in S82X1940 is part of the NLR ionized by the AGN. In all the cases presented above, we do not rule out the possibility of a companion galaxy in a merger with the AGN host galaxy.

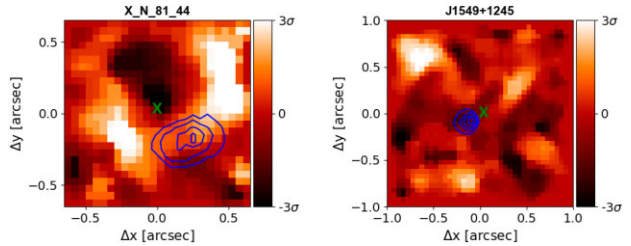

Figure 6. Same as Fig. 5 but for targets, X_N_81_44 and J1549+1245, that do not show the same location of the [O III] and Hα emission.

In summary, out of the 16 type 1 AGN in the SUPER survey that show extended Hα emission, four galaxies (∼25, ∼18 per cent if we include all type 1 AGN, including unresolved galaxies) show that the extended Hα emission is most likely ionized by star formation and in five galaxies (∼30, ∼23 per cent if all the type 1 AGN are included) the ionization is dominated by the AGN. In the remaining seven galaxies, the ionization source of the extended Hα emission remains unconstrained. In two galaxies (cid_346 and S82X1940), the width of the Hα line >600 km s^{-1}, suggesting that the Hα emission is tracing ionized outflow driven by the AGN. However, we cannot exclude the possibility that the turbulence in the ISM is related to an ongoing merger event, for which higher resolution and deeper data are required. We also note that the width alone should not be used as an indicator for star forming or AGN origin to the emission, as the spectra extracted from extended emission line regions are highly limited by noise.

From the analysis presented in this section, we conclude that Hα emission in high redshift galaxies does not necessarily trace star formation, but can also be associated with AGN ionization or outflows or possible companions.

3.4 Impact of ionized outflows on unobscured star formation

To quantify the impact that ionized outflows may have on star formation, we compare the spatial locations of ionized outflows, traced using the [O III] emission presented in Kakkad et al. (2020), with the extended Hα emission presented in this paper. We perform this analysis on targets where both the [O III] and the Hα emission is extended. Furthermore, we limit this analysis to those targets where the extended Hα emission is consistent with ionization by star formation, in order to use it as a tracer of short time-scale (∼10 Myr) unobscured star formation. Based on the analysis presented in Sections 3.2 and 3.3, two targets fulfil these criteria: X_N_81_44 and X_N_66_23. Fig. 7 shows the extended Hα map tracing star formation in these two targets, overlaid by [O III]-based outflow velocity contours in blue. Only the contours with [O III]w_{80} values above 600 km s^{-1} are shown in Fig. 7. The astrometry of the *H*-band and *K*-band images was registered using the AGN continuum peak emission in the respective data cubes.

We observe a spatial anticorrelation between the locations of high velocity [O III] outflows (w_{80} >600 km s^{-1}) and unobscured star formation in X_N_81_44 and X_N_66_23. These results might suggest that star formation is being actively shut down in regions with high-velocity outflows, a result also previously reported in the literature (e.g. Cano-Díaz et al. 2012; Carniani et al. 2016). However, we cannot rule out a scenario where the high-velocity winds compress gas ahead of it, resulting in triggering of star formation in the edges of the outflow (e.g. Cresci et al. 2015). We note here that the spatial anticorrelation between high velocity outflows and Hα emission is observed only in the PSF-subtracted Hα images and not in the narrow Hα maps obtained using the pixel-by-pixel fit, which will be described in Section 4. The left-hand panel in Fig. 8 shows the Hα flux map of X_N_81_44, obtained from the narrow Gaussian component, which shows that most of the emission is concentrated close to the AGN location. However, the emission close to the AGN is dominated by the PSF smearing effect. The right-hand panel, on the other hand, shows the PSF-subtracted Hα channel map, which removes any emission that might be affected by beam smearing, as described earlier in Section 3.2. The results in Fig. 8 may explain some of the observed differences, such as the presence or absence of such spatial anticorrelations found in other high-z AGN host galaxies (e.g. Carniani et al. 2016; Scholtz et al. 2021).

We note that the spatial resolution of the SINFONI observations prevents us from investigating the morphology of the Hα emission within the 2 kpc PSF element which was subtracted in the maps shown in Fig. 7. In other words, the SINFONI data are unable to trace star formation on scales smaller than 2 kpc at these redshifts and therefore we cannot exclude the presence of ongoing star formation in the central cavity in the maps in Fig. 7. Observations with upcoming facilities such as ELT/HARMONI will provide the necessary spatial resolution to resolve regions in sub-kiloparsec scales in these galaxies, where there could possibly be underlying emission from the host galaxy.

In X_N_81_44, we also compare the outflow locations with archival high resolution (∼0.2 arcsec) ALMA Band 7 (870 μm observed frame, ∼260 μm rest frame) dust continuum maps from Lamperti et al. (2021). The dust continuum emission is overlaid as red contours in Fig. 7. The spectral energy distribution (SED) analysis of X_N_81_44 suggests that >99 per cent of the rest frame 260 μm emission is from dust heated by star formation and <1 per cent contribution from the AGN-heated dust and synchrotron emission (see Lamperti et al. 2021). We can therefore use the dust continuum maps to trace longer time-scale star formation from dust reheated by the UV radiation from stars over the last ∼100 Myrs.

High-redshift galaxies are known to host copious amount of dust, which can have a significant impact on how we interpret the results on the spatial distribution of outflow versus star formation (e.g. Fujimoto et al. 2018; Lamperti et al. 2021; Scholtz et al. 2021). Star formation tracers using rest frame optical emission lines, such as Hα, are susceptible to dust obscuration and previous work has shown that the dust distribution (obtained from far-infrared ALMA observations, for instance) and Hα distributions (or rest-frame optical continuum distribution in case of narrow band *HST* observations) are different in high-redshift galaxies (Hodge et al. 2016; Lang et al. 2019; Chen et al. 2020). In general, Hα distributions tend to be more extended compared to the dust emission. There is a large concentration of star formation dominated infrared emission at the centre of galaxies that one needs to account for (e.g. Hao et al. 2011). This is the case also for the ALMA dust continuum emission (red contours) for X_N_81_44 (left-hand panel in Fig. 7) that peaks in the central region and extends towards the Hα emission in the SE direction from the AGN. Therefore, based on the ALMA map, there is no clear anticorrelation between the location of the ionized outflow and regions with active star formation. However, we note that the dust obscured star formation traced by sub-mm or far-infrared observations represents star formation over long time-scales of ∼100 Myrs. On the contrary, the outflow time-scale is much shorter (10^5 to a few Myrs; e.g. Schawinski et al. 2015). Therefore, we cannot exclude that the possible impact of the outflow on star formation may be diluted by the large time range to which the star formation is sensitive. Furthermore, the ALMA dust-continuum

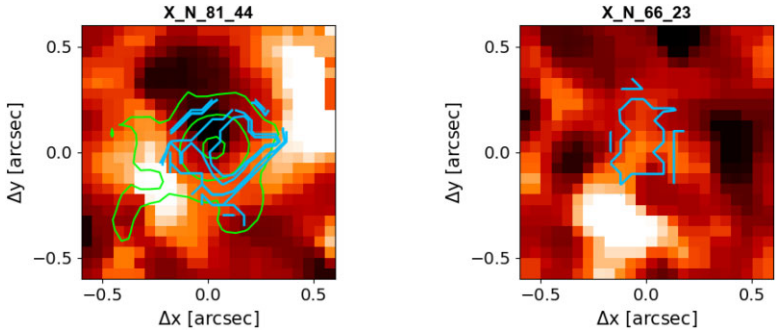

Figure 7. The figure shows the spatial locations of the H α emission and [O III] based ionized outflows in X_N_81_44 (left-hand panel) and X_N_66_23 (right-hand panel). The background image shows the PSF-subtracted H α images from the maps in Fig. 2. The blue contours trace the [O III] outflows ($w_{80} >$ 600 km s^{-1}) at levels 600, 700, and 750 km s^{-1} in X_N_81_44; and 850 and 1050 km s^{-1} in X_N_66_23. The extended H α emission in these galaxies is absent in the direction with highest w_{80} values. The green contours in X_N_81_44 show the archival ALMA band 7 dust continuum emission (from Lamperti et al. 2021), that traces dust reheated star formation. The implications of these observations are further discussed in Section 3.3.

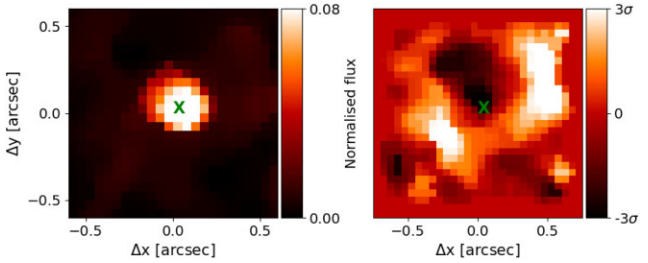

Figure 8. The left-hand panel shows the narrow H α flux map of X_N_81_44 obtained from the pixel-by-pixel Gaussian fit of the H α complex. The right-hand panel, on the other hand, shows the PSF-subtracted H α channel map of the same target. The figure highlights that the PSF dominates the bulk of the emission close to the AGN location (marked by the black star).

observations (Lamperti et al. 2021) were not able to resolve spatial scales below ∼2 kpc and therefore we cannot exclude the presence of cavities below this physical scale. This limitation could be mitigated with spatially resolved mid-infrared observations with JWST/MIRI.

4 KINEMATIC PROPERTIES OF NARROW H α EMISSION

In this section, we describe the pixel-by-pixel H α emission line modelling for the targets that show extended H α emission after subtracting the PSF, as described earlier in Section 3.2. We primarily derive the kinematic maps from the BLR component-subtracted emission line models, namely the H α centroid map (also called moment 1 map) and non-parametric velocity and velocity dispersion maps i.e. v_{10} and w_{80} maps (see e.g. Harrison et al. 2014; Cresci et al. 2015). We compare these H α maps with that of the [O III] emission in the *H*-band data to determine whether the H α emission mimics the kinematics of the [O III] emitting gas. This comparison can be used to further distinguish between a star formation or NLR origin to the H α emission.

As described earlier in Section 3.1, the H α complex is composed of several Gaussian functions, each representing the individual components of the H α and [N II]λλ6549, 6585 emission lines. To avoid degeneracy during the pixel-by-pixel fit, we employ the following constraints on the individual Gaussian components to model the spatial distribution of the narrow component of the H α emission, conventionally treated as tracing the host galaxy star formation. All the constraints described here are fixed or varied relative to the integrated spectrum fitting results using the M3 model, as described in Section 3.1. As the BLR emission is unresolved, we fix the centroid and the width of the BLR components and only allow a variation in its peak value. In all but two targets (cid_346 and S82X1940), the spectrum extracted from the extended regions in the PSF-subtracted cube shows an H α width (FWHM) of <600 km s^{-1}. In these targets where the H α FWHM < 600 km s^{-1}, we fix the centroid and width of the broad NLR component and only allow a variation in its peak (similar to the constraint imposed on the BLR component). The centroid, width, and the peak of the narrow NLR component of the H α line are allowed to vary across the field of view. In the case of cid_346 and S82X1940, we also allow small variations in the broad NLR component.

We attempt the pixel-by-pixel analysis of the H α line only for the 15 targets that show extended H α emission from the analysis presented in Section 3.2. Out of these 15 targets, 4 targets (X_N_53_3, X_N_66_23, cid_166 and cid_1605) did not have sufficient S/N per pixel to constrain the parameters of individual Gaussian components. We note that deriving the PSF-subtracted maps was possible despite the low S/N in these four targets as we relied on the channel maps and not on Gaussian fits to verify the presence or absence of residuals. The H α complex in the case of J1333+1649 is contaminated by telluric features in the wings of the profile and in the case of J1549+1245, the individual Gaussian components remained unconstrained, which made the pixel-by-pixel analysis for these two targets unreliable. Fig. 9 shows an example of the line fitting in individual pixels for X_N_115_23 as an example.

In Fig 10, we show the BLR-subtracted H α kinematic maps of X_N_160_22, X_N_115_23, cid_346 and S82X2058 as examples, while similar plots for other targets are moved to the Appendix A. The left-hand panels in Fig. 10 show the H α centroid map, the middle panel shows the 10th percentile velocity, v_{10}, and the right-hand panel shows the H α width containing 80 per cent of the line flux. The kinematic centre for the centroid map is obtained from the location of the narrow H α emission in the integrated spectrum (Section 3.1). Folding the information derived in Section 3.3, we now discuss the possible origin of the observed kinematic properties of the H α line. We attempt to distinguish between rotating disc signatures, mergers, and outflowing components. For a rotationally supported disc, we expect a smooth gradient in the line centroid maps and a centrally peaked velocity dispersion (in this case, w_{80}). On the other hand, galaxies undergoing mergers or outflows will not necessarily show a centrally peaked velocity dispersion map and/or an ordered

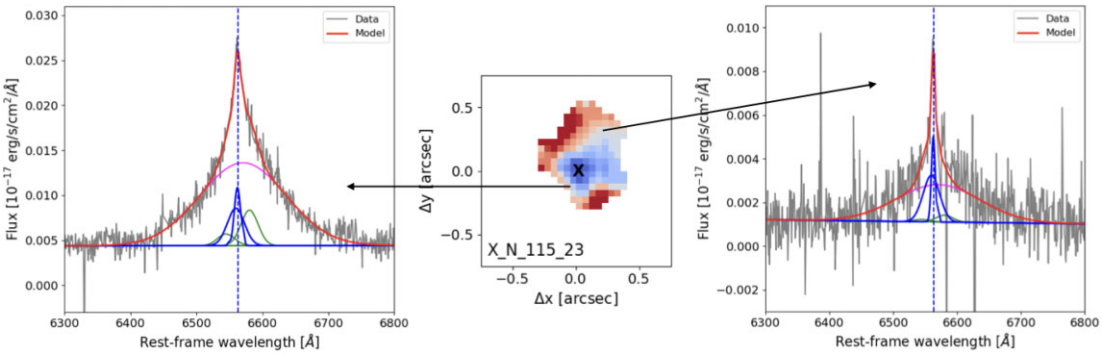

Figure 9. An example of line modelling in individual pixels in X_N_115_23. The middle panel shows the H α centroid map and the left- and right-hand panels show the extracted spectrum and the emission line model in two pixels located by the arrows.

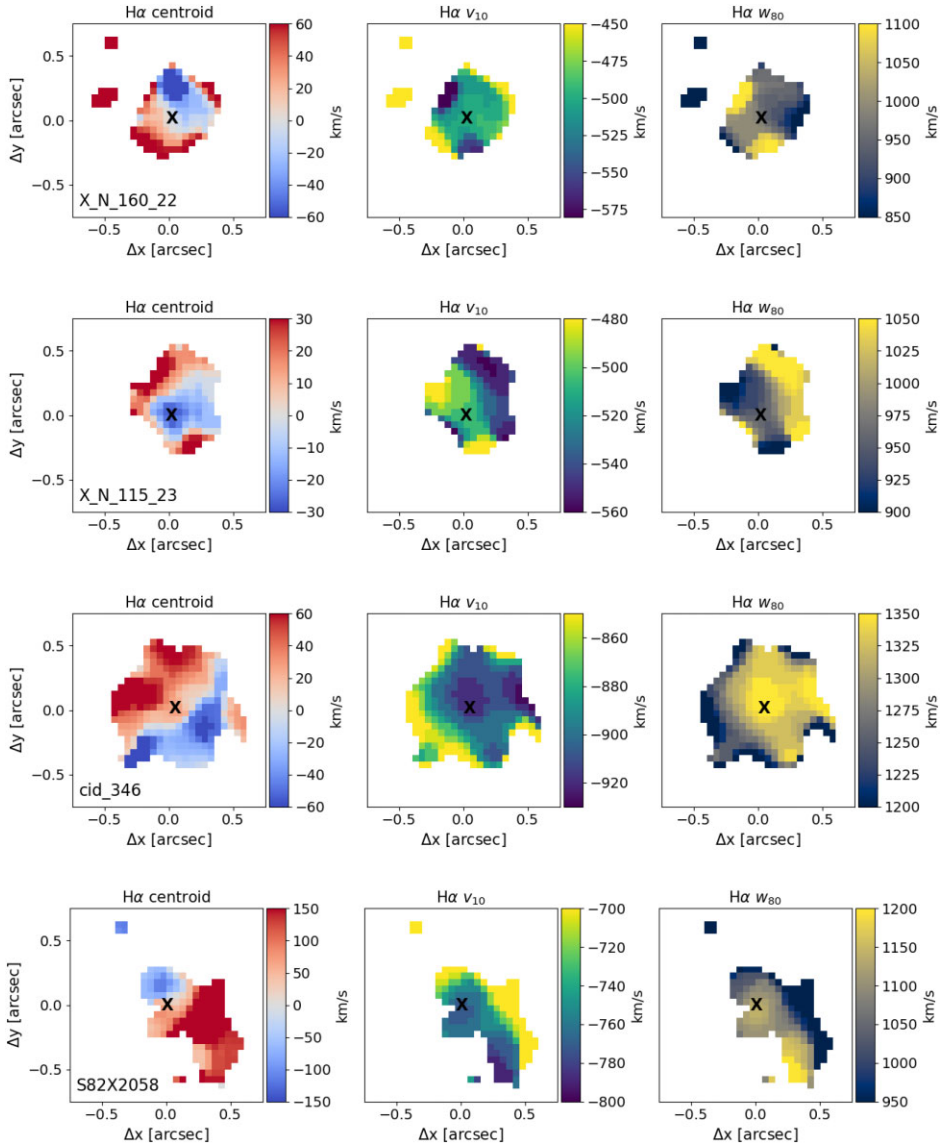

Figure 10. H α NLR component velocity maps of (from top to bottom) X_N_160_22, X_N_115_23, cid_346, and S82X2058 as examples. The plots for the rest of the targets are moved to the appendix A (Fig. A3). The left-hand panels show the H α centroid map, the middle panels the v_{10} map and the right-hand panels the w_{80} maps. The targets show a diverse set of H α velocity distributions. X_N_160_22, cid_346, and S82X2058 show smooth velocity gradients in their H α centroid profiles. S82X2058 shows an extended structure towards the SW of the nucleus, suggesting a possible faint companion. The H α centroid profile of X_N_115_23 does not show a smooth rotation-like velocity gradient as in other galaxies, which is consistent with the finding that the extended H α emission is a part of the NLR (Fig. 2). These maps are discussed further in Section 4.

velocity gradient in the centroid map. We discuss a few examples of targets shown in Fig. 10.

X_N_160_22 does not show extended [O III] emission, but shows extended H α emission towards the north of the AGN location, evident in the PSF-subtracted H α channel map in Fig. 2 and the centroid map in the left-hand panel of Fig. 10. The centroid map shows a smooth velocity gradient between ±60 km s^{-1}. The v_{10} and w_{80} maps show maximum velocities of <-600 and >1000 km s^{-1}, suggesting the presence of AGN outflows, especially close to the AGN location. Considering that the extended H α emission is consistent with star formation, the H α velocity maps of X_N_160_22 in Fig. 10 could be interpreted as a superposition of a rotating medium (centroid map that shows a smooth gradient) and a turbulent medium (v_{10} and w_{80} maps that show high velocities near the AGN location).

In the case of X_N_115_23, the H α centroid value at the AGN location appears blue-shifted and the w_{80} map does not show a centrally peaked profile, but shows a smooth gradient. The velocities in the w_{80} map reaches values between ∼850 and >1000 km s^{-1} suggesting that H α emission is tracing gas which is part of an outflow in the NLR. This is also supported by the fact that the H α and [O III] emission are spatially extended in the same direction and that the extended emission is ionized by the AGN (see BPT map in Fig. 5).

cid_346 shows a smooth velocity gradient in the centroid map with the major axis orientated roughly along the NE direction and the w_{80} map peaks at ∼1300 km s^{-1} at the AGN location. The large dispersion value cannot be explained purely as ordered rotation and therefore we infer that the observed H α emission is a combination of rotation from the host galaxy and AGN outflows. Although the extended H α emission in this galaxy falls under the AGN ionized region in Fig. 5, the presence of upper limits in the [N II]/H α ratio could suggest that star formation may play a role in the ionization and kinematics of the observed extended emission. However, the current data does not allow us to definitely confirm this.

Lastly, S82X2058 shows a smooth velocity gradient in its H α centroid map, but the centroid velocity profile is extended more towards the SE direction from the AGN location. Accounting for the localized peak in the w_{80} map at the AGN location, this target shows a rotating system probably in an interaction with another galaxy.

To summarize the results on the spatially resolved kinematic analysis of the H α line: Six galaxies (X_N_160_22, X_N_81_44, X_N_4_48, cid_346, S82X1940, and S82X2058) show smooth velocity gradients in their H α centroid maps. The velocity dispersion maps in these galaxies (w_{80}) show localized peaks.[1] This suggests that in these six galaxies, part or most of the H α emission traces the rotating gas. On the contrary, X_N_12_26, X_N_115_23, and S82X1905 do not have smooth gradients in their centroid maps. The extended H α emission in X_N_115_23 and S82X1905 is consistent with ionization by the AGN (Section 3.3) and therefore the absence of smooth gradient in the H α centroid profile confirms that the H α emission is dominated by AGN emission. The extended H α emission in X_N_12_26 is highly asymmetric around the AGN location, which may suggest the presence of companion galaxies. This is not a unique case: from the H α kinematic maps, there are indications of companions also in the case of X_N_4_48, S82X1940, and S82X2058.

Several galaxies presented in this paper show extended H α emission blue-shifted or redshifted by several hundred km s^{-1} compared to the systemic values. For instance, J1549+1245 shows

[1]The w_{80} maps are sensitive to the line models derived from the multiple Gaussian fits. Also the IFU data is noise limited, especially in the outskirts of the galaxies, and therefore the spatial profiles in these velocity might not always look smooth, but can suggest underlying patterns.

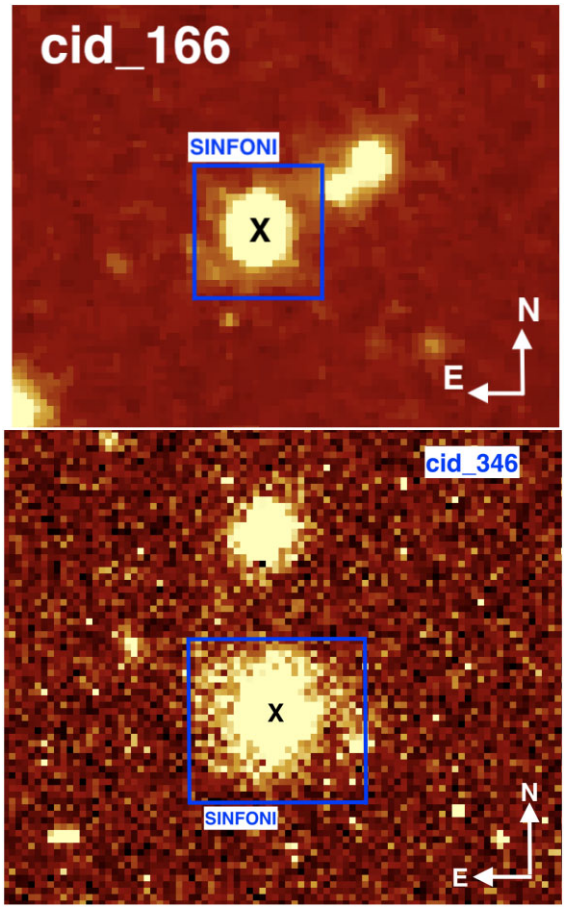

Figure 11. Archival *HST*/WFC3 images of cid_166 (top panel) and cid_346 (bottom panel), both type 1 AGN in the SUPER survey. The *HST* images are obtained with the F160W filter (near-infrared) and both the images suggest the presence of a companion. The cid_166 image clearly shows a stream linking the two galaxies. The blue square in each of the panels show the SINFONI 3 arcsec × 3 arcsec FoV. Therefore, current observations presented in this paper do not capture the presence of these companions.

an extended H α component at ∼10 kpc from the AGN location, but this component is red-shifted by ∼1800 km s^{-1} on extracting the spectra (Fig. 3). Although the presence of large scale outflows cannot be ruled out in this case, the presence of such extended components might also suggest the presence of companions or the AGN host galaxies in the process of a merger. Observations of some of the type 1 SUPER AGN in other wavelengths already suggest the presence of companions. For instance, recent ALMA CO(4-3) observations of J1549+1245 confirmed the presence of a companion at $>3\sigma$ significance (see Bischetti et al. 2021) and therefore the observed extended H α could be a part of a tidal tail. Furthermore, archival *HST* observations of cid_166 and cid_346 already indicate possible presence of galaxies nearby (Fig. 11), which suggests that galaxy interactions may be a common phenomenon at these redshifts. We note here that cid_346 is surrounded by an extended CO halo, which could also point to an overdensity of galaxies around this source (see Cicone et al. 2021). Although AGN hosted in interacting systems have been reported to be rare at $1 < z < 2$ (e.g. Cisternas et al. 2011; Mainieri et al. 2011), this may also be due to observational biases or the limitation to obtain better spatial resolution and high sensitivity at high redshift. In fact, recent ALMA observations have revealed evidence of quasars residing in interacting galaxies (e.g. Trakhtenbrot et al. 2017; Banerji et al. 2021).

5 SUMMARY AND CONCLUSIONS

We presented the spatially resolved properties of the Hα emission from the *K*-band ($\sim$2–2.4 μm) VLT/SINFONI observations of 21 type 1 AGN at z $\sim$ 2.2 derived from the SUPER survey. The adaptive optics assisted observations provided a spatial resolution of $\sim$2 kpc that allowed us to infer the source of ionization in the extended Hα regions, after accounting for beam-smearing effects due to the PSF. We used resolved BPT analysis, [N II]/Hα ratios of the extended emission and a comparison between the Hα kinematics with that of the [O III] emission, obtained from the *H*-band observations presented in Kakkad et al. (2020), to infer if the Hα emission traces star formation. Lastly, we investigate if star-forming regions and high velocity ionized outflows are spatially anticorrelated. The main results of this paper are summarized below:

(i) We tested three methods of Hα emission line modelling in this paper because the blending of [N II]$\lambda\lambda$6549, 6585 and Hα emission line components in the integrated spectra of type 1 AGN host galaxies at z $\sim$ 2 can lead to degenerate results. We conclude that in order to obtain unique solutions, the kinematic components of the Hα emission need to be coupled with the [O III] emission.

(ii) The vast majority of the quasars show extended Hα emission ($\sim$76 per cent). The extended emission is observed out to $\sim$3–9 kpc with a mean value of $\sim$5 kpc. The width (FWHM) of the Hα spectrum, extracted from the extended regions, is in the range 73–784 km s^{-1} with a mean width of 312 km s^{-1}.

(iii) We find a correlation between the velocity shift, defined by the difference between the extended Hα location in the spectra with the expected location based on its redshift, with the AGN luminosity and black hole mass. This could indicate that the extended Hα emission is dominated by outflowing gas. The size of the extended Hα emission, on the other hand, shows possible correlations with the stellar mass of the host galaxy, consistent with size-mass relations reported in the literature.

(iv) In four galaxies, we were able to constrain the flux ratios [O III]/Hβ and [N II]/Hα at the location of extended Hα emission and place them on the classical BPT maps. The Hα emission in these four galaxies is consistent with ionization by star formation. For the rest of the targets, we use [N II]/Hα ratio and the Hα FWHM to identify the source of ionization. Overall, the extended Hα emission in four galaxies is consistent with ionization by star formation ($\sim$25 per cent of the targets that show extended emission), in five galaxies by the AGN ($\sim$30 per cent) and in seven galaxies, the ionization source could not be constrained ($\sim$45 per cent).

(v) We find a variety of dynamical properties in the host galaxies as traced by the Hα emission. Six out of nine galaxies for which pixel-by-pixel emission line fitting was possible show smooth velocity gradients in the Hα centroid maps and their BPT diagrams are also consistent with ionization by star formation, suggesting that the Hα emission traces the host rotation and not the NLR. In two galaxies, the Hα morphology and kinematic maps are similar to that of [O III] and along with the fact that their BPT location is consistent with AGN ionization, the Hα emission in these two galaxies traces the NLR. In four galaxies, the morphological and kinematic characteristics of the Hα emission may indicate the presence of companions or AGN hosts being in mergers.

(vi) In two galaxies, we find evidence of negative AGN feedback on scales >2 kpc as the extended Hα emission in these galaxies avoid regions with high velocity [O III]-based ionized outflows. For the rest of the targets, there is no strong evidence of AGN outflows having an impact on the host galaxy star formation using the current data. ALMA Band 7 observations of a fraction of galaxies show the prevalence of dust heated star formation at the centre of the galaxy close to the AGN and the ionized outflow. The current SINFONI observations are not sensitive to resolutions <2 kpc therefore future high spatial resolution observations with ELT-class IFS instruments such as HARMONI will be required to constrain the real impact of the outflows by sampling recent star formation in the proximity of the AGN location.

The current SINFONI *K*-band observations of most of the galaxies in the SUPER survey have an on-source exposure time of $\sim$1–2 h. Deeper observations are therefore required with current or future facilities such as rest-frame *HST*/FUV imaging, VLT/ERIS, VLT/HAWKI-GRAAL, and ELT/HARMONI to distinguish between the presence of outflows/inflows and possible presence of companions. Finally, upcoming JWST observations in Cycle-1 (ID 2177) will use the mid-infrared IFS capabilities of JWST/MIRI (e.g. Rieke et al. 2015), that will allow us to detect dust-obscured star formation using the PAH 6.2 μm emission, at a spatial resolution similar to those of SINFONI observations presented in this paper.

ACKNOWLEDGEMENTS

The authors would like to thank the anonymous referee for comments that improved the paper. CMH acknowledges funding from a United Kingdom Research and Innovation grant (code: MR/V022830/1). AP gratefully acknowledges financial support from Science and Technology Facilities Council (STFC) through grants ST/T000244/1 and ST/P000541/1. Based on observations collected at the European organization for Astronomical Research in the Southern Hemisphere under ESO programme 196.A-0377. For the purpose of open access, the authors have applied a Creative Commons Attribution (CC-BY) license to any author accepted version arising.

DATA AVAILABILITY

The IFS data products will be made publicly available via ESO Phase 3 data release. The raw data can be retreived from the ESO archive: archive.eso.org under the programme ID 196.A-0377.

REFERENCES

Alaghband-Zadeh S., Banerji M., Hewett P. C., McMahon R. G., 2016, MNRAS, 459, 999
Alatalo K. et al., 2015, ApJ, 798, 31
Baldwin J. A., Phillips M. M., Terlevich R., 1981, PASP, 93, 5
Balmaverde B. et al., 2016, A&A, 585, A148
Banerji M., Jones G. C., Carniani S., DeGraf C., Wagg J., 2021, MNRAS, 503, 5583
Baron D. et al., 2018, MNRAS, 480, 3993
Baron D., Netzer H., Davies R. I., Xavier Prochaska J., 2020, MNRAS, 494, 5396
Battisti A. J., Calzetti D., Johnson B. D., Elbaz D., 2015, ApJ, 800, 143
Beckmann R. S. et al., 2017, MNRAS, 472, 949
Bessiere P. S., Ramos Almeida C., 2022, MNRAS, 512, L54
Bieri R., Dubois Y., Silk J., Mamon G. A., Gaibler V., 2016, MNRAS, 455, 4166
Bischetti M. et al., 2017, A&A, 598, A122
Bischetti M. et al., 2021, A&A, 645, A33
Boquien M. et al., 2015, A&A, 578, A8
Brusa M. et al., 2016, A&A, 588, A58
Brusa M. et al., 2018, A&A, 612, A29
Caglar T. et al., 2020, A&A, 634, A114
Calzetti D., 2020, Nat. Astron., 4, 437
Cano-Díaz M., Maiolino R., Marconi A., Netzer H., Shemmer O., Cresci G., 2012, A&A, 537, L8
Carniani S. et al., 2015, A&A, 580, A102

Carniani S. et al., 2016, A&A, 591, A28
Carniani S. et al., 2017, A&A, 605, A105
Catalán-Torrecilla C. et al., 2015, A&A, 584, A87
Chen C.-C. et al., 2020, A&A, 635, A119
Cicone C. et al., 2021, A&A, 654, L8
Circosta C. et al., 2018, A&A, 620, A82
Circosta C. et al., 2021, A&A, 646, A96
Cisternas M. et al., 2011, ApJ, 726, 57
Civano F. et al., 2016, ApJ, 819, 62
Costa T., Rosdahl J., Sijacki D., Haehnelt M. G., 2018, MNRAS, 473, 4197
Cresci G., Maiolino R., 2018, Nat. Astron., 2, 179
Cresci G. et al., 2015, ApJ, 799, 82
Davies R. et al., 2020, MNRAS, 498, 4150
Dubois Y., Gavazzi R., Peirani S., Silk J., 2013, MNRAS, 433, 3297
Dubois Y., Peirani S., Pichon C., Devriendt J., Gavazzi R., Welker C., Volonteri M., 2016, MNRAS, 463, 3948
Dugan Z., Bryan S., Gaibler V., Silk J., Haas M., 2014, ApJ, 796, 113
Eisenhauer F. et al., 2003, in Iye M., Moorwood A. F. M., eds, Proc. SPIE Conf. Ser. Vol. 4841, Instrument Design and Performance for Optical/Infrared Ground-based Telescopes. SPIE, Bellingham, p. 1548
Ellison S. L. et al., 2021, MNRAS, 505, L46
Fabian A. C., 2012, ARA&A, 50, 455
Fiore F. et al., 2017, A&A, 601, A143
Fluetsch A. et al., 2019, MNRAS, 483, 4586
Förster Schreiber N. M., Wuyts S., 2020, ARA&A, 58, 661
Förster Schreiber N. M. et al., 2018, ApJS, 238, 21
Fujimoto S. et al., 2018, ApJ, 861, 7
Gabor J. M., Bournaud F., 2014, MNRAS, 441, 1615
Gaibler V., Khochfar S., Krause M., Silk J., 2012, MNRAS, 425, 438
Gallagher R., Maiolino R., Belfiore F., Drory N., Riffel R., Riffel R. A., 2019, MNRAS, 485, 3409
Gatkine P., Veilleux S., Perley D., Durbak J., Dichiara S., Cenko S. B., Troja E., 2022, ApJ, 926, 63
Gebhardt K. et al., 2000, ApJ, 539, L13
Georgakakis A., Nandra K., 2011, MNRAS, 414, 992
George K. et al., 2019, MNRAS, 487, 3102
Greene J. E., Zakamska N. L., Ho L. C., Barth A. J., 2011, ApJ, 732, 9
Guillard P., Boulanger F., Lehnert M. D., Pineau des Forêts G., Combes F., Falgarone E., Bernard-Salas J., 2015, A&A, 574, A32
Gültekin K. et al., 2009, ApJ, 698, 198
Hao C.-N., Kennicutt R. C., Johnson B. D., Calzetti D., Dale D. A., Moustakas J., 2011, ApJ, 741, 124
Harrison C. M., Alexander D. M., Mullaney J. R., Swinbank A. M., 2014, MNRAS, 441, 3306
Harrison C. M., Costa T., Tadhunter C. N., Flütsch A., Kakkad D., Perna M., Vietri G., 2018, Nat. Astron., 2, 198
Hirschmann M., Dolag K., Saro A., Bachmann L., Borgani S., Burkert A., 2014, MNRAS, 442, 2304
Hodge J. A. et al., 2016, ApJ, 833, 103
Hopkins A. M., Beacom J. F., 2006, ApJ, 651, 142
Husemann B., Scharwächter J., Bennert V. N., Mainieri V., Woo J. H., Kakkad D., 2016, A&A, 594, A44
Husemann B., Davis T. A., Jahnke K., Dannerbauer H., Urrutia T., Hodge J., 2017, MNRAS, 470, 1570
Ishibashi W., Fabian A. C., 2012, MNRAS, 427, 2998
Jahnke K., Wisotzki L., Sánchez S. F., Christensen L., Becker T., Kelz A., Roth M. M., 2004, Astron. Nachr., 325, 128
Jarvis M. E. et al., 2020, MNRAS, 498, 1560
Kakkad D. et al., 2016, A&A, 592, A148
Kakkad D. et al., 2017, MNRAS, 468, 4205
Kakkad D. et al., 2020, A&A, 642, A147
Kakkad D. et al., 2022, MNRAS, 511, 2105
Kalfountzou E. et al., 2017, MNRAS, 471, 28
Kauffmann G. et al., 2003, MNRAS, 346, 1055
Kennicutt Jr R. C., 1998, ARA&A, 36, 189
Kewley L. J., Dopita M. A., Leitherer C., Davé R., Yuan T., Allen M., Groves B., Sutherland R., 2013, ApJ, 774, 100
Kim C. et al., 2022, ApJ, 928, 19
Kormendy J., Richstone D., 1995, ARA&A, 33, 581
Koss M. J. et al., 2021, ApJS, 252, 29
LaMassa S. M. et al., 2016, ApJ, 817, 172
Lamperti I. et al., 2021, A&A, 654, A90
Lang P. et al., 2019, ApJ, 879, 54
Liu Z. et al., 2016, MNRAS, 459, 1602
Luo B. et al., 2017, ApJS, 228, 2
Luo R., Woo J.-H., Shin J., Kang D., Bae H.-J., Karouzos M., 2019, ApJ, 874, 99
Mainieri V. et al., 2011, A&A, 535, A80
Mainieri V. et al., 2021, Messenger, 182, 45
Maiolino R. et al., 2017, Nature, 544, 202
Man A. W. S., Lehnert M. D., Vernet J. D. R., De Breuck C., Falkendal T., 2019, A&A, 624, A81
Menzel M. L. et al., 2016, MNRAS, 457, 110
Michiyama T., Iono D., Nakanishi K., Ueda J., Saito T., Yamashita T., Bolatto A., Yun M., 2020, ApJ, 895, 85
Nesvadba N. P. H., Bicknell G. V., Mukherjee D., Wagner A. Y., 2020, A&A, 639, L13
Osterbrock D. E., Ferland G. J., 2006, Astrophysics of gaseous nebulae and active galactic nuclei
Perna M. et al., 2015, A&A, 574, A82
Perna M. et al., 2020, A&A, 643, A139
Perna M. et al., 2021, A&A, 646, A101
Pillepich A. et al., 2018, MNRAS, 473, 4077
Puglisi A. et al., 2021, Nat. Astron., 5, 319
Ramos Almeida C. et al., 2021, A&A, 658, 29
Rauch M., Becker G. D., Haehnelt M. G., Carswell R. F., Gauthier J. R., 2013, MNRAS, 431, L68
Richstone D. et al., 1998, Nature, 385, A14
Rieke G. H. et al., 2015, PASP, 127, 584
Rojas A. F. et al., 2020, MNRAS, 491, 5867
Roos O., Juneau S., Bournaud F., Gabor J. M., 2015, ApJ, 800, 19
Rosario D. J. et al., 2018, MNRAS, 473, 5658
Salomé Q., Salomé P., Combes F., 2015, A&A, 574, A34
Schawinski K., Koss M., Berney S., Sartori L. F., 2015, MNRAS, 451, 2517
Schaye J. et al., 2015, MNRAS, 446, 521
Scholtz J. et al., 2020, MNRAS, 492, 3194
Scholtz J. et al., 2021, MNRAS, 505, 5469
Schutte Z., Reines A. E., 2022, Nature, 601, 329
Shin J., Woo J.-H., Chung A., Baek J., Cho K., Kang D., Bae H.-J., 2019, ApJ, 881, 147
Shivaei I. et al., 2016, ApJ, 820, L23
Silk J., 2013, ApJ, 772, 112
Silk J., Rees M. J., 1998, A&A, 331, L1
Soltan A., 1982, MNRAS, 200, 115
Springel V., 2005, MNRAS, 364, 1105
Steinborn L. K., Dolag K., Hirschmann M., Prieto M. A., Remus R.-S., 2015, MNRAS, 448, 1504
Tozzi G. et al., 2021, A&A, 648, A99
Trakhtenbrot B., Lira P., Netzer H., Cicone C., Maiolino R., Shemmer O., 2017, ApJ, 836, 8
Veilleux S., Osterbrock D. E., 1987, ApJS, 63, 295
Venturi G. et al., 2018, A&A, 619, A74
Vietri G. et al., 2018, A&A, 617, A81
Vietri G. et al., 2020, A&A, 644, A175
Vietri G. et al., 2022, A&A, 659, A129
Vogelsberger M. et al., 2014, MNRAS, 444, 1518
Ward S. R., Harrison C. M., Costa T., Mainieri V., 2022, MNRAS, 514, 2936
White S. D. M., Rees M. J., 1978, MNRAS, 183, 341
Xie Y., Ho L. C., 2019, ApJ, 884, 136
Yu Q., Tremaine S., 2002, MNRAS, 335, 965
Zubovas K., Bourne M. A., 2017, MNRAS, 468, 4956
Zubovas K., Nayakshin S., Sazonov S., Sunyaev R., 2013a, MNRAS, 431, 793
Zubovas K., Nayakshin S., King A., Wilkinson M., 2013b, MNRAS, 433, 3079
van der Wel A. et al., 2014, ApJ, 788, 28

APPENDIX A: LINE FITTING RESULTS USING DIFFERENT METHODS

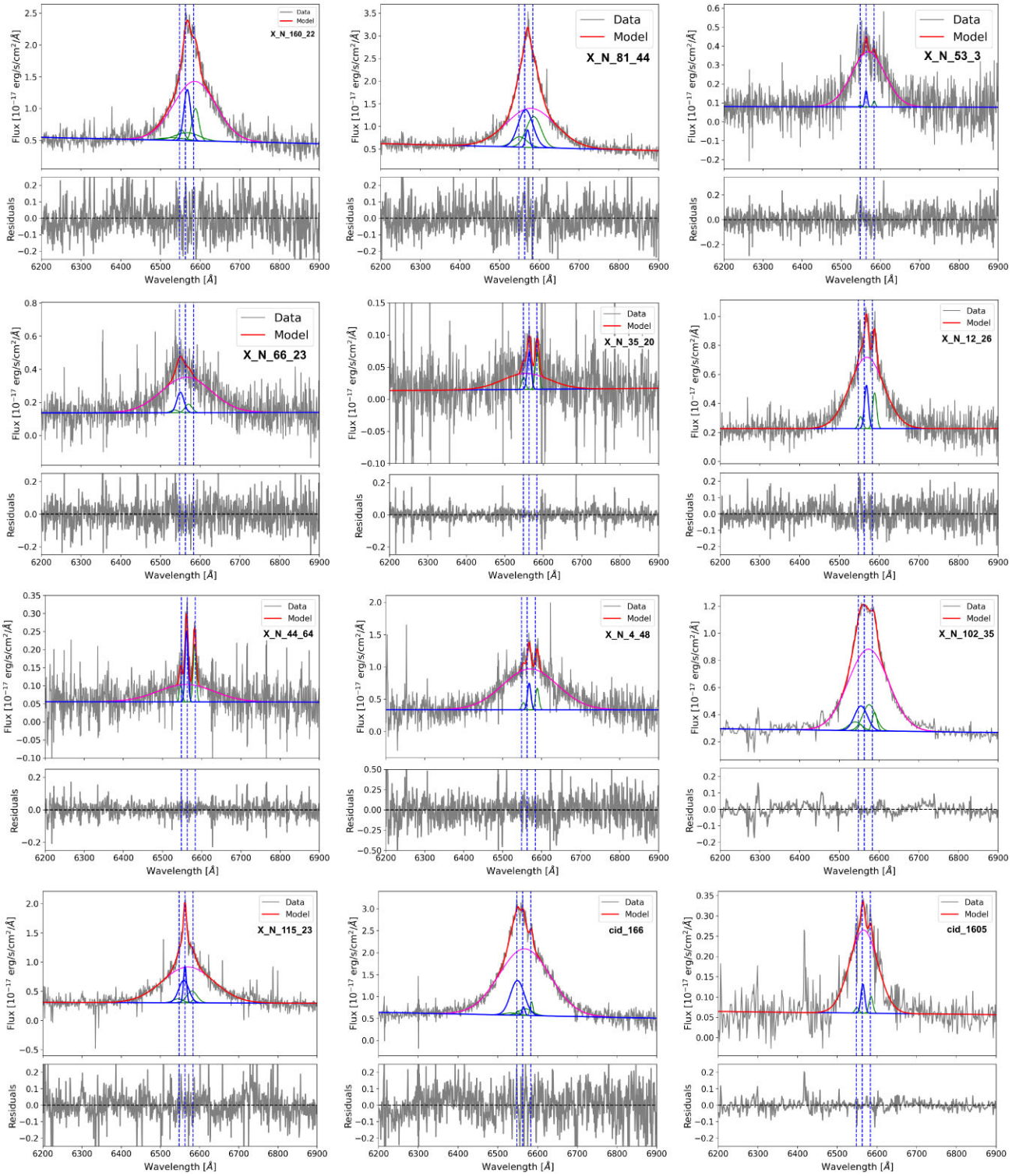

Figure A1. Integrated K-band spectra of all targets for the fitting model used in this paper.

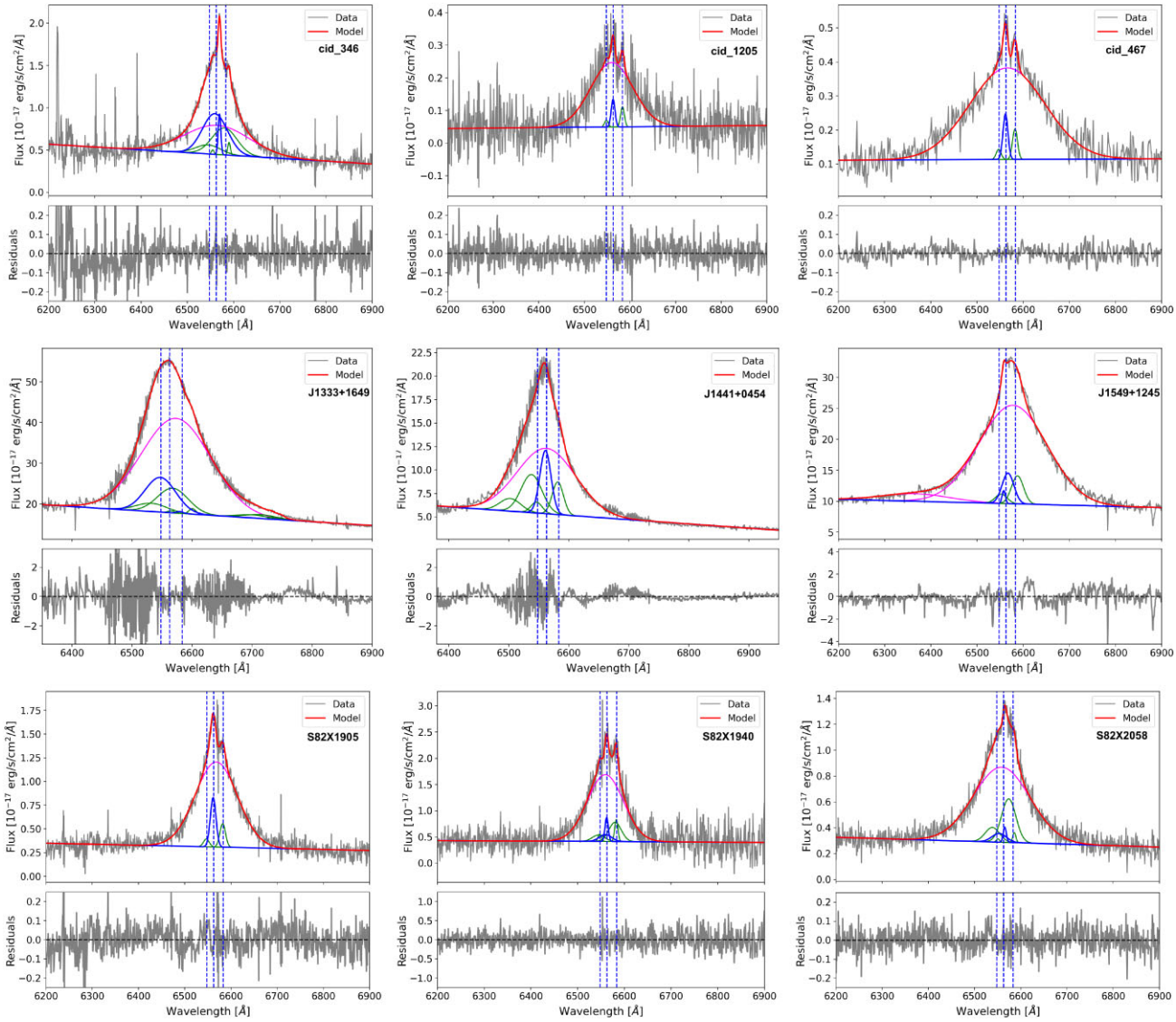

Figure A2. Integrated *K*-band spectra of all targets for the fitting model used in this paper (continued from Fig. A1).

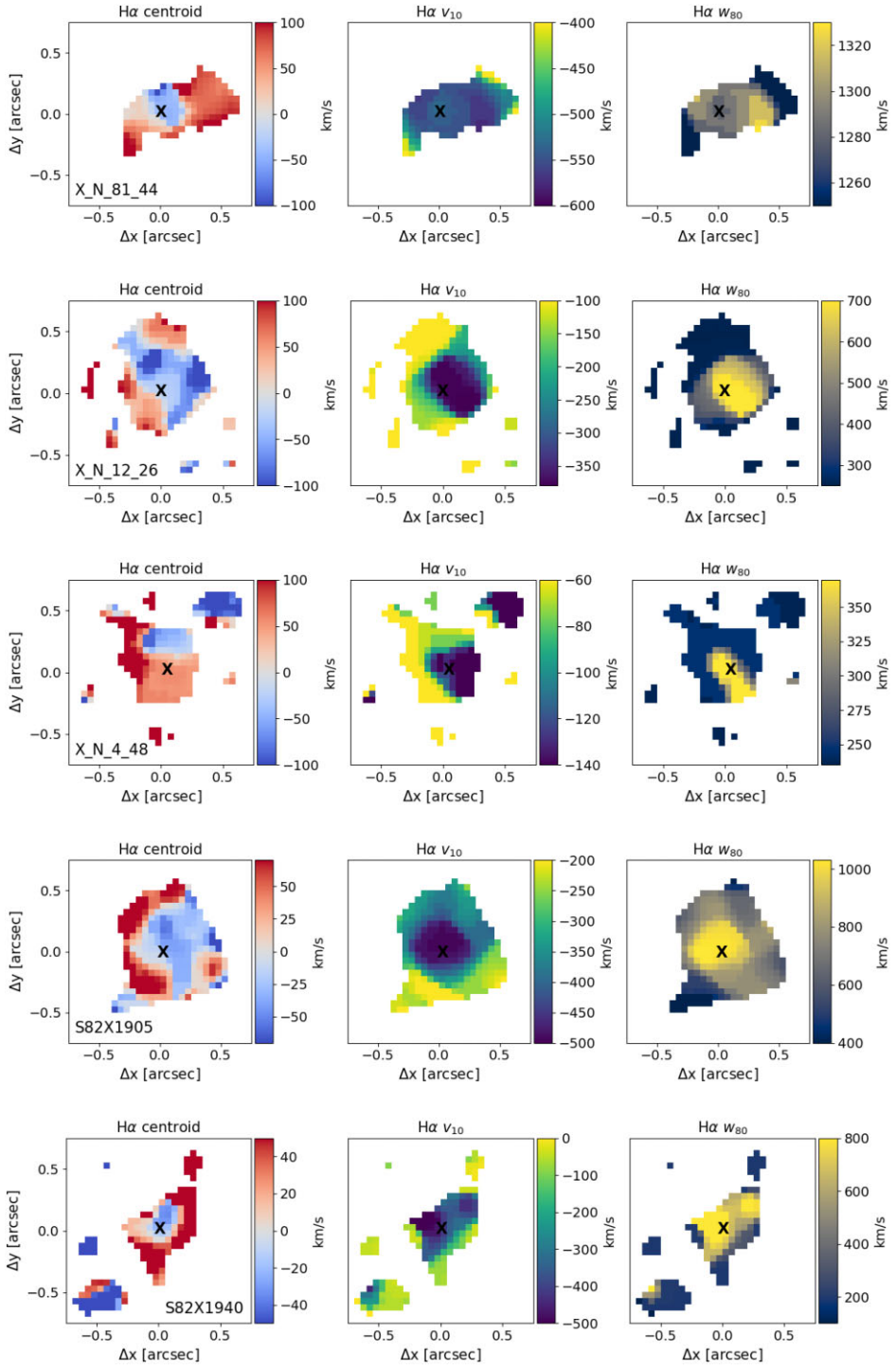

Figure A3. Same as Fig. 10.

Table A1. H α line fitting parameters for the M2 model. The line fitting for J1441+0454 remained unconstrained and hence not reported in this table.

Target	λ_{range}	Aperture	FWHM			$L_{H\alpha}$		
			v_1	v_2	v_{BLR}	L_1	L_2	L_{BLR}
	Å	arcsec	km s^{-1}	km s^{-1}	km s^{-1}	erg s^{-1}	erg s^{-1}	erg s^{-1}
X_N_160_22	6200–6900	0.9	287 ± 53	2211 ± 278	6807 ± 260	42.68 ± 0.13	43.84 ± 2.90	44.28 ± 0.01
X_N_81_44	6200–6900	0.9	990 ± 82	2929 ± 95	8250 ± 313	43.27 ± 0.06	44.02 ± 0.14	44.16 ± 0.02
X_N_53_3	6200–6900	0.8	345 ± 213	–	4577 ± 187	42.04 ± 0.22	–	43.70 ± 0.01
X_N_66_23	6200–6900	0.9	–	–	5640 ± 182	–	–	43.72 ± 0.01
X_N_35_20	6200–6900	0.5	532 ± 63	–	6549 ± 972	41.97 ± 0.06	–	42.68 ± 0.05
X_N_12_26	6200-6900	1.0	544 ± 32	–	4615 ± 100	42.80 ± 0.04	–	43.95 ± 0.01
X_N_44_64	6200–6900	0.5	411 ± 17	–	7688 ± 560	42.37 ± 0.02	–	43.03 ± 0.02
X_N_4_48	6200–6900	0.7	473 ± 53	–	7596 ± 303	42.79 ± 0.06	–	44.18 ± 0.01
X_N_102_35	6200–6900	0.3	535 ± 151	3443 ± 92	9070 ± 588	–	43.71 ± 0.17	43.67 ± 0.02
X_N_115_23	6200–6900	0.9	376 ± 52	1184 ± 139	6862 ± 162	42.85 ± 0.11	43.25 ± 0.07	44.16 ± 0.01
cid_166	6200–6900	0.9	458 ± 49	1968 ± 260	6943 ± 95	42.66 ± 0.16	43.77 ± 0.13	44.60 ± 0.01
cid_1605	6200–6900	0.3	516 ± 110	–	3802 ± 80	41.96 ± 0.15	–	43.27 ± 0.01
cid_346	6200–6900	0.9	301 ± 43	2884 ± 156	7298 ± 592	42.60 ± 0.08	43.60 ± 0.16	43.89 ± 0.05
cid_1205	6200–6900	0.8	446 ± 89	–	5023 ± 183	42.04 ± 0.12	–	43.46 ± 0.01
cid_467	6200–6900	0.3	575 ± 61	–	8750 ± 285	42.37 ± 0.05	–	43.86 ± 0.01
J1333+1649	6350–7000	0.9	1059 ± 415	4246 ± 320	8839 ± 304	43.87 ± 0.16	45.28 ± 3.27	45.30 ± 0.03
J1549+1245	6200–6900	1.1	1045 ± 35	4557 ± 118	10495 ± 208	44.23 ± 0.02	41.73 ± 3.87	45.50 ± 0.01
S82X1905	6200–6900	1.0	920 ± 58	–	5219 ± 96	43.14 ± 0.03	–	44.11 ± 0.01
S82X1940	6200–6900	0.8	426 ± 117	3001 ± 713	6430 ± 1138	42.78 ± 1.45	43.15 ± 4.49	43.69 ± 0.28
S82X2058	6200-6900	0.9	481 ± 75	3243 ± 192	8809 ± 455	42.43 ± 0.11	40.88 ± 3.82	43.95 ± 0.03

Table A2. H α line fitting parameters for the M1 model. The emission line modelling using the M1 method for J1441+0454 and J1549+1245 remained unconstrained. Only those targets are shown for which the line fitting results were different from the ones in Table A1 i.e. for those targets where only H α components were sufficient to reproduce the H α complex.

Target	λ_{range}	Aperture	FWHM			$L_{H\alpha}$		
			v_1	v_2	v_{BLR}	L_1	L_2	L_{BLR}
	Å	arcsec	km s^{-1}	km s^{-1}	km s^{-1}	erg s^{-1}	erg s^{-1}	erg s^{-1}
X_N_160_22	6200–6900	0.9	296 ± 44	2368 ± 60	6742 ± 188	42.68 ± 0.07	43.95 ± 0.02	44.28 ± 0.01
X_N_81_44	6200–6900	0.9	1034 ± 65	3168 ± 104	8336 ± 321	43.31 ± 0.05	44.17 ± 0.02	44.15 ± 0.02
X_N_53_3	6200–6900	0.8	1527 ± 623	–	4718 ± 266	42.71 ± 0.52	–	43.66 ± 0.02
X_N_66_23	6200–6900	0.9	150 ± 150	–	5638 ± 167	41.44 ± 0.33	–	43.72 ± 0.01
X_N_115_23	6200–6900	0.9	527 ± 27	3306 ± 114	9339 ± 344	43.10 ± 0.02	43.82 ± 0.03	44.10 ± 0.02
cid_1605	6200–6900	0.3	1200 ± 409	–	3887 ± 217	42.26 ± 0.35	–	43.27 ± 0.02
J1333+1649	6350–7000	0.9	2354 ± 657	4444 ± 909	9058 ± 492	44.47 ± 0.33	45.38 ± 3.01	45.30 ± 0.05

[1]*Space Telescope Science Institute, 3700 San Martin Drive, Baltimore, MD 21218, USA*
[2]*European Southern Observatory, Alonso de Cordova 3107, Vitacura, Casilla, 19001 Santiago de Chile, Chile*
[3]*Department of Physics, University of Oxford, Denys Wilkinson Building, Keble Road, Oxford OX1 3RH, UK*
[4]*European Southern Observatory, Karl-Schwarzschild-Strasse 2, Garching bei München, 85748, Germany*
[5]*INAF - Osservatorio Astronomico di Roma, Via Frascati 33 00040, Monte Porzio Catone, Italy*
[6]*INAF - Istituto di Astrofisica Spaziale e Fisica Cosmica Milano, Via A. Corti 12, 20133 Milano, Italy*
[7]*Centro de Astrobiología (CAB), CSIC–INTA, Ctra. de Ajalvir Km. 4, 28850 Torrejón de Ardoz, Madrid, Spain*
[8]*Scuola Normale Superiore, Piazza dei Cavalieri 7, I-56126 Pisa, Italy*
[9]*INAF - Osservatorio Astrofisico di Arcetri, Largo E. Fermi 5, 50125 Firenze, Italy*
[10]*School of Mathematics, Statistics and Physics, Newcastle University, Newcastle upon Tyne NE1 7RU, UK*

[11]*Dipartimento di Fisica e Astronomia, Universitá di Firenze, Via G. Sansone 1, Sesto Fiorentino, 50019 Firenze, Italy*
[12]*Dipartimento di Fisica, Universitá di Trieste, Sezione di Astronomia, Via G.B. Tiepolo 11, I-34131 Trieste, Italy*
[13]*INAF - Osservatorio Astronomico di Trieste, Via G. Tiepolo 11, I-34143 Trieste, Italy*
[14]*Institute of Theoretical Astrophysics, University of Oslo, PO Box 1029, Blindern 0315, Oslo, Norway*
[15]*Department of Physics & Astronomy, University College London, Gower Street, London WC1E 6BT, UK*
[16]*European Space Agency (ESA), European Space Astronomy Centre (ESAC), Camino Bajo del Castillo s/n, 28692 Villanueva de la Cañada, Madrid, Spain*
[17]*Max-Planck-Institut für Astronomie, Königstuhl 17, D-69117 Heidelberg, Germany*
[18]*Dunlap Institute for Astronomy and Astrophysics, University of Toronto, 50 St George Street, Toronto ON M5S 3H4, Canada*
[19]*Department of Physics & Astronomy, University of British Columbia, 6224 Agricultural Road, Vancouver BC V6T 1Z1, Canada*
[20]*School of Physics and Astronomy, Tel-Aviv University, Tel Aviv 69978, Israel*
[21]*Affiliated to INAF-Osservatorio di Astrofisica e Scienza dello Spazio, Via Piero Gobetti 93/3, I-40129 Bologna, Italy*
[22]*Centre for Extragalactic Astronomy, Department of Physics, Durham University, South Road, Durham DH1 3LE, UK*
[23]*Kavli Institute for Cosmology, University of Cambridge, Madingley Road, Cambridge CB3 0HA, UK*
[24]*Cavendish Laboratory - Astrophysics Group, University of Cambridge, 19 JJ Thompson Avenue, Cambridge CB3 0HE, UK*
[25]*Dipartimento di Fisica e Astronomia 'Augusto Righi', Universitá degli Studi di Bologna, via P. Gobetti, 93/2, 40129 Bologna, Italy*
[26]*INAF-Osservatorio di Astrofisica e Scienza dello Spazio di Bologna, via Piero Gobetti, 93/3, I-40129 Bologna, Italy*

This paper has been typeset from a TEX/LATEX file prepared by the author.